Fuel 427 (2027) 139480

Contents lists available at ScienceDirect

Fuel

journal homepage: www.elsevier.com/locate/jfue

Full length article

Entrained flow gasification: Surrogate slag property data for model validation

Maximilian Dammann[a, b, c, *], Stella Clara Walker[a, b], Michael Müller[d], Ulrike Santo[b], Hannah Knoch[b], Mark Eberhard[b], Marco Mancini[c], Thomas Kolb[a, b]

[a] Karlsruhe Institute of Technology (KIT), Engler-Bunte-Institute, Fuel Technology (EBI ceb), Engler-Bunte-Ring 1, 76131 Karlsruhe, Germany
[b] Karlsruhe Institute of Technology (KIT), Institute for Technical Chemistry, Gasification Technology (ITC vgt), Hermann-von-Helmholtz-Platz 1, 76344 Eggenstein-Leopoldshafen, Germany
[c] Clausthal University of Technology, Institute for Energy Process Engineering and Fuel Technology (IEVB), Agricolastraße 4, 38678 Clausthal-Zellerfeld, Germany
[d] Forschungszentrum Jülich, Institute of Energy Materials and Devices, Structure and Function of Materials (IMD-1), Wilhelm-Johnen-Straße, 52425 Jülich, Germany

HIGHLIGHTS

- Complete and consistent glass slag property data are provided for slag flow modelling.
- Thickness of glass slag deposition was measured after reactor shut-down.
- One-dimensional slag layer model is employed based on derived slag property data.
- Slag thickness is analysed based on measured and predicted data.
- Slag temperature is studied using derived slag thermal conductivity data.

ARTICLE INFO

Keywords:
Entrained flow
Gasification
Slag
Properties
Modelling
Simulation

ABSTRACT

Slag deposition and slag drain restrict the operating and process conditions of entrained flow gasifiers that are operated on ash-containing fuels. Numerical simulations of these gasifiers require mathematical models to describe slag deposition and slag flow. Previous studies, however, have not provided complete and consistent slag property data for the development and validation of slag flow models. Therefore, a preceding study (Fuel 382 A (2025) 132809) carried out pilot-scale entrained flow gasification experiments at the bioliq Entrained Flow Gasifier (bioliq EFG) plant. The membrane-wall reactor of this plant is equipped with a segmental cooling screen, which was recoated before the experiments to ensure well-defined heat transfer conditions. The experiments were conducted with mixtures of ethylene glycol and glass beads as well as pyrolysis oil and glass beads at thermal inputs of up to 5 MW and operating pressures of 40 bar. Ethylene glycol and glass beads were used as surrogates for pyrolysis oil and straw ash, respectively, in order to derive experimental data under well-defined conditions for the development and validation of slag flow models. This study investigated deposited and discharged glass slags from the pilot-scale experiments. Samples of slag deposited on the membrane-wall refractory were analysed for density and morphology, while samples of discharged slag were analysed for chemical composition, melting behaviour, density, surface tension, morphology, dynamic viscosity, thermal conductivity and specific heat capacity. In addition, the thickness of the slag depositions was measured after reactor shut-down. The analyses and measurements provided complete and consistent data for the development of slag layer and slag flow models. The predictions of one-dimensional slag layer simulations showed good to fair agreement with the measured slag thickness data.

* Corresponding author.
Email address: maximilian.dammann@kit.edu (M. Dammann).

https://doi.org/10.1016/j.fuel.2026.139480
Received 9 January 2026; Received in revised form 21 March 2026; Accepted 12 April 2026
Available online 27 May 2026

Nomenclature

Latin symbols

A	area
$\hat{C}_p$	specific isobaric heat capacity
d	thickness
h	heat transfer coefficient
l	length
p	pressure
P_{th}	thermal input
$\dot{q}$	heat flux
$\dot{Q}$	heat flow rate
r	radius
T	temperature
w	mass fraction
x	mole fraction

Greek symbols

γ	surface tension
ϵ	emissivity
η	dynamic viscosity
λ	stoichiometric ratio
λ	thermal conductivity
ρ	density
σ	Stefan–Boltzmann constant

Subscripts and superscripts

ash	of ash
B	at position B
bal	balanced
C	at position C
CFD	based on CFD simulation
conv	convective
dry	on dry basis
exp	experimental
FT	fluid
gas	gas, gas-side
HT	hemispherical
i	inner
IDT	initial deformation
max	maximum
mean	mean
meas	measured
min	minimum
ng	of natural gas
o	outer
op	operating
rad	radiative
s	surface
S2	of segment 2
S3	of segment 3
slag	of slag, in slag
slurry	of slurry
SST	average sintering
ST	softening
steam	of steam
tot	total
wall	wall
water	water, water-side
WGS	water-gas-shift

Acronyms

bioliq EFG	bioliq Entrained Flow Gasifier
CFD	computational fluid dynamics
ICP-OES	inductively coupled plasma optical emission spectrometry
KIT	Karlsruhe Institute of Technology
N1998	following DIN 51730:1998 [1]
N2007	following DIN 51730:2007 [2]
SEM	scanning electron microscope
SPH	smoothed-particle-hydrodynamics
VoF	volume-of-fluid
WGS	water-gas-shift
XRD	X-ray diffraction
XRFS	X-ray fluorescence spectroscopy
ZAE	Zentrum für Angewandte Energieforschung
1D	one-dimensional

1. Introduction

Entrained flow gasification of biogenic and anthropogenic feedstocks can be used for producing renewable liquid fuels and chemicals in a circular economy and reducing CO_2 emissions [3–5]. First, the feedstocks are pyrolysed and converted to suspension fuels with high mineral contents [3]. Then, the suspension fuels are disintegrated using gasification media and converted to synthesis gas, while the molten mineral fuel compounds deposit, together with soot and incompletely converted carbonaceous particles, on the refractory and form liquid, crystalline and solidified slag phases [6,7]. The slag protects the refractory against corrosion under reducing conditions at high temperatures and pressures but also restricts the operating and process conditions due to its material properties [6,7]. For example, the slag surface tension influences the slag deposition through the adhesion of particles on slag or refractory [7–11]. The slag thermal conductivity and heat capacity, in turn, determine the temperature distribution (in both slag and refractory) and thus the heat extraction [7]. The slag viscosity and density finally affect the flow behaviour [7,12–15], as thick viscous slags can block the gasifier outlet at lower temperatures, whereas thin viscous slags can quickly drain at higher temperatures. The analysis of the slag properties is therefore crucial for the understanding and mathematical description of slag deposition and slag flow, and hence the design and operation of entrained flow gasifiers [7].

Numerous studies [8,10–13,15–60] have already analysed slag deposition and slag flow using simplified balance equations or advanced methods. The simplified balance equations have primarily been based on the gravity-driven steady-state film flow model, while the advanced methods have included the volume-of-fluid (VoF) method or the smoothed-particle-hydrodynamics (SPH) method. Most of previous studies focussed on model application and sensitivity analysis and described the slag properties based on measured chemical compositions and on literature data and correlations [7,15,61–71]. In addition, several studies [15,17,29,30,34,36,38,45,48,49,51,53–55,57] derived customised slag viscosity relationships from high-temperature measurements. Finally, Zhang et al. [50] determined area porosities of up to 10% using scanning electron microscope (SEM) analyses of slag samples in order to account for physical gas enclosures in the slag flow model. The development of slag deposition and slag flow models is thus typically coupled with a few experimental analyses only. This is because measurements of density, surface tension, viscosity, thermal conductivity and heat capacity require higher expenditures than analyses of composition and melting behaviour, which are frequently done for operational reasons. So far, Mills and Rhine [67,68] and Seebold et al. [7] derived larger data sets for entrained flow gasifier slags. Mills and Rhine [67,68] investigated density, thermal expansion, dynamic viscosity, thermal conductivity, thermal diffusivity, specific heat capacity, surface tension, total normal emissivity and extinction coefficient of

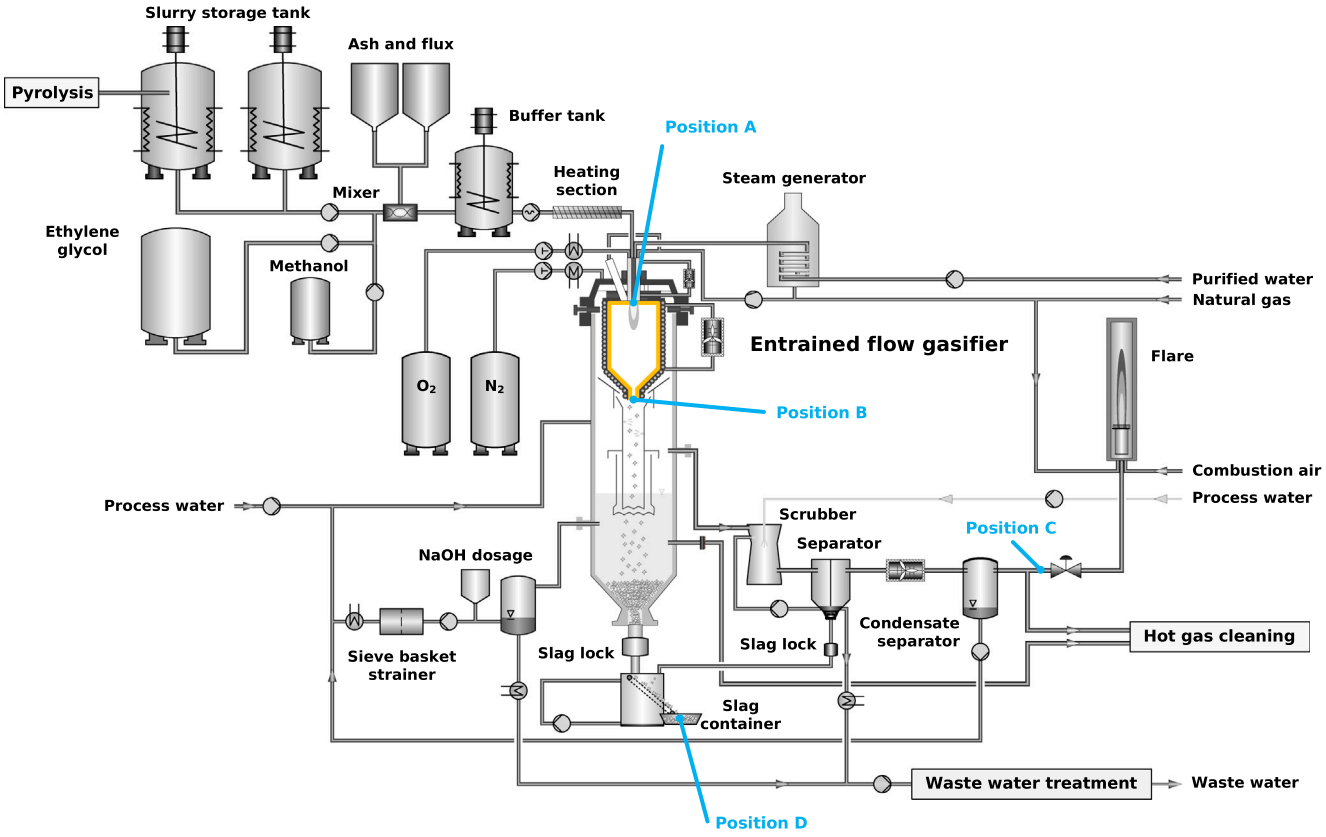

Fig. 1. Process flow-sheet of the high-pressure gasification of the bioliq pilot plant including the bioliq EFG, the system boundary of the inner reactor chamber (depicted with a yellow border) and characteristic positions A, B, C and D [4,6,116] (For interpretation of the references to colour in this figure legend, the reader is referred to the web version of this article.).

various coal gasifier slags. Seebold et al. [7] measured density, surface tension, dynamic viscosity and specific heat capacity of two biomass slags. For lack of alternatives, these data sets were adopted in several numerical studies [15,19–21,23,28,30,32–34,36,38,48,50,60].

Furthermore, a few studies [48,49,51,58–60] attempted to validate their predictions of slag deposition with measurement data. Xu et al. [49] and Lin et al. [58,59] showed a good agreement of predicted outer wall temperatures with measured industrial data. Safronov et al. [48] reported a good agreement of predicted slag thicknesses with unpublished industrial data. In addition, Seebold et al. [7], Cavagnol et al. [51] and Dammann et al. [60] presented measured slag thicknesses from pilot-scale entrained flow gasification experiments at the bioliq Entrained Flow Gasifier (bioliq EFG) plant (see Fig. 1). The data were determined under ambient conditions after reactor shut-down [7,51,60] and were only in fair agreement with predictions [60]. The discrepancies were linked to imperfect particle tracking, inappropriate material property data and slag drain during shut-down [60].

In summary, previous studies have not yet succeeded in the development of a validated slag flow model based on consistent slag property models. Moreover, several studies [10,11,23,26,27,31,36,43,44] emphasised the need of validation experiments. Therefore, a preceding study [6] conducted four pilot-scale entrained flow gasification experiments at the bioliq EFG plant after recoating the cooling screen and derived input and validation data for CFD models. These data comprise measured refractory temperatures, derived gas temperatures, measured and derived gas-species concentrations, balanced heat extractions and further characteristic parameters (e. g. carbon conversions and cold-gas efficiencies). The present study has subsequently focussed on the characterisation of glass slags, that were formed and discharged in the pilot-scale experiments, in order to provide complete and consistent material property and deposition data for the development and validation of slag flow and high-pressure entrained flow gasification models. First, the thickness of the slag depositions was measured under ambient conditions after completing the experiments. Then, samples of slag deposited on the refractory were analysed for density and morphology, while samples of discharged slag were analysed for chemical composition, melting behaviour, density, surface tension, morphology, dynamic viscosity, thermal conductivity and specific heat capacity. Finally, one-dimensional slag layer simulations were conducted to verify the measured slag thicknesses and to analyse the predictions. The pilot-scale experiments are introduced in Section 2. The methods and the results of the experimental and numerical analyses are described in Sections 3 and 4. The measured and derived slag property data and various predictions for slag and wall layers are discussed in Section 5. The conclusions are given in Section 6.

2. Pilot-scale experiments

This study presents slag property data that were generated in the course of the bioliq EFG experiments V82, V83, V84 and V85 [6]. These four experiments were conducted at the high-pressure entrained flow gasifier of the bioliq pilot plant (nowadays the CCLab) of Karlsruhe Institute of Technology (KIT). The membrane-wall gasifier is operated at 40 bar and is equipped with a segmental cooling screen. The refractory of the cooling screen was renewed before the experiments to ensure well-defined heat transfer conditions [6]. Characteristic operating and process parameters of the experiments are summarised in Tables 1 and 2. The bioliq EFG experiments V82, V83 and V84 were conducted with mixtures of ethylene glycol and glass beads (stationary input for at least 6 h), while the bioliq EFG experiment V85 was carried out with beech wood

Table 1
Characteristic operating and process parameters [6]: feedstocks, thermal inputs of slurry $P_{th,slurry}$, thermal inputs of natural gas $P_{th,ng}$, operating pressures p_{op}, ash/slurry mass flow rate ratios $\dot{m}_{ash}/\dot{m}_{slurry}$, steam/slurry mass flow rate ratios $\dot{m}_{steam}/\dot{m}_{slurry}$, oxygen/slurry mass flow rate ratios $\dot{m}_{O_2}/\dot{m}_{slurry}$ and stoichiometric ratios λ.

Experiment	Feedstock	$\frac{P_{th,slurry}}{MW}$	$\frac{P_{th,ng}}{MW}$	$\frac{p_{op}}{bar}$	$\frac{\dot{m}_{ash}}{\dot{m}_{slurry}}$	$\frac{\dot{m}_{steam}}{\dot{m}_{slurry}}$	$\frac{\dot{m}_{O_2}}{\dot{m}_{slurry}}$	λ
V82	Ethylene glycol + glass beads	3.5	0.5	40	0.045	0.38	0.79	0.553
V83	Ethylene glycol + glass beads	3.5	0.5	40	0.045	0.38	0.74	0.521
V84	Ethylene glycol + glass beads	3.3	0.5	40	0.090	0.38	0.78	0.571
V85	Beech wood pyrolysis oil + glass beads	4.4	0.5	40	0.046	0.40	0.88	0.465

Table 2
Process parameters [6] for slag layer simulations: balanced temperatures at position B $T_{bal,B}$, WGS temperatures at position B $T_{WGS,B}$, total heat extractions $\dot{Q}_{tot}$, heat extractions through segment 2 $\dot{Q}_{S2}$, heat extractions through segment 3 $\dot{Q}_{S3}$, average water temperatures in segment 2 $T_{water,S2}$, average water temperatures in segment 3 $T_{water,S3}$, average convective water-side heat transfer coefficients in segment 2 $h_{water,S2}$ and average convective water-side heat transfer coefficients in segment 3 $h_{water,S3}$.

Experiment	Feedstock	$\frac{T_{bal,B}}{K}$	$\frac{T_{WGS,B}}{K}$	$\frac{\dot{Q}_{tot}}{kW}$	$\frac{\dot{Q}_{S2}}{kW}$	$\frac{\dot{Q}_{S3}}{kW}$	$\frac{T_{water,S2}}{K}$	$\frac{T_{water,S3}}{K}$	$\frac{h_{water,S2}}{W/(m^2K)}$	$\frac{h_{water,S3}}{W/(m^2K)}$
V82	Ethylene glycol + glass beads	1621	1537	544.51	154.90	212.27	490	493	16,595	16,004
V83	Ethylene glycol + glass beads	1607	1546	445.81	133.89	185.99	489	492	16,602	16,029
V84	Ethylene glycol + glass beads	1667	1617	524.13	154.84	208.88	490	493	16,451	15,871
V85	Beech wood pyrolysis oil + glass beads	1672	1607	477.83	143.58	190.77	490	492	16,602	15,904

pyrolysis oil and glass beads (stationary input for 100 h) [6]. Ethylene glycol and glass beads were used as surrogates for pyrolysis oil and straw ash, respectively, in order to enable reproducible experiments with well-defined chemical and physical properties of the feedstock [6,60,72]. Ethylene glycol exhibits a C/H/O ratio and a heating value similar to typical biomass pyrolysis oils [6,73], while the glass beads exhibit low catalytic activities compared to biomass ash and were employed to ensure slag deposition and protection of the refractory material of the cooling screen [6]. The glass beads with particle sizes ranging from 5 µm to 80 µm were purchased from Arteka [74]. The bioliq EFG experiment V82 was defined as near-equilibrium reference experiment with high carbon conversions and low methane concentrations, whereas the bioliq EFG experiments V83 and V84 were used to investigate the influence of a lower stoichiometric ratio and a higher glass content on the process conditions, respectively [6]. The bioliq EFG experiments were operated at almost equal operating pressures and synthesis gas flow rates resulting in thermal inputs between 3.8 MW and 4.9 MW. More details on the bioliq EFG and the bioliq EFG experiments V82, V83, V84 and V85 are given in the preceding studies [4,6].

3. Methods

This section describes the methods used for the experimental slag and the experimental and numerical slag deposition analyses.

3.1. Samples

The samples were collected primarily at position D of the bioliq EFG plant (see Fig. 1). Sampling errors are possible but are likely small, particularly when compared to uncertainties in the measurement methods and the material variability. Therefore, the samples are assumed to be representative for the discharged slags and were pulverised, melted, degassed and finally analysed to determine chemical composition and melting behaviour. In addition, degassed samples discharged in the bioliq EFG experiment V82 were prepared to measure density, morphology, surface tension, dynamic viscosity, thermal conductivity and specific heat capacity. Furthermore, several samples were taken at the refractory positions MP6, MP5, MP1-4 and MP7 (see Fig. 2) after the bioliq EFG experiment V82. These samples were used to investigate physical gas enclosures through density and morphology analyses. For simplicity, the samples of both discharged and deposited slag are hereinafter also referred to as slags or glass slags.

3.2. Chemical analyses

The compositions of the discharged slags V82, V83, V84 and V85 were determined using X-ray fluorescence spectroscopy (XRFS), while the composition of the glass beads was analysed using both XRFS and inductively coupled plasma optical emission spectrometry (ICP-OES). The XRFS analyses were carried out based on DIN 51729-11:1998 [76] at the Institute for Technical Chemistry, Mineralogy of Karlsruhe Institute of Technology, while accounting for drift corrections and using two different calibrations (C2016 and C2019). The ICP-OES analyses were conducted based on DIN EN ISO 11885:2009 [77] at Eurofins [78].

3.3. Melting analyses

The melting analyses of the glass beads and the discharged slags V82, V83, V84 and V85 were used to determine the average sintering temperatures T_{SST}, the initial deformation temperatures T_{IDT}, the softening temperatures T_{ST}, the hemispherical temperatures T_{HT} and the fluid temperatures T_{FT}. The characteristic melting temperatures were obtained using a heating microscope (Hesse Instruments EM301) under a reducing atmosphere following DIN 51730:1998 [1] (N1998) at the Institute for Technical Chemistry, Pyrolysis/Gas Treatment of Karlsruhe Institute of Technology or following DIN 51730:2007 [2] (N2007) at Eurofins [78]. Firstly, glass beads or pulverised discharged glass slag samples were pressed to cylindrical samples. Then, grey-scale images of the samples were recorded, while heating the samples up to 1823 K using a heating rate of 10 K/min between 873 K and 1823 K. The recorded images were evaluated to derive the characteristic melting temperatures.

3.4. Density measurements at ambient temperatures and morphology analyses

The density at ambient temperatures and the morphology were analysed to investigate physical gas enclosures in the solidified slag samples, recalling that (i) the bioliq EFG experiments were conducted at high-pressure conditions, (ii) the gas solubility increases with increasing pressure and decreases with increasing temperature, and (iii) bubbles, trapped or formed during the reaction of captured carbon on molten slag surface, diffuse in the liquid slag [79] and affect the slag properties [50]. Specifically, glass beads and samples of slag V82, collected at positions D, MP6, MP5, MP1-4 and MP7, were examined using helium

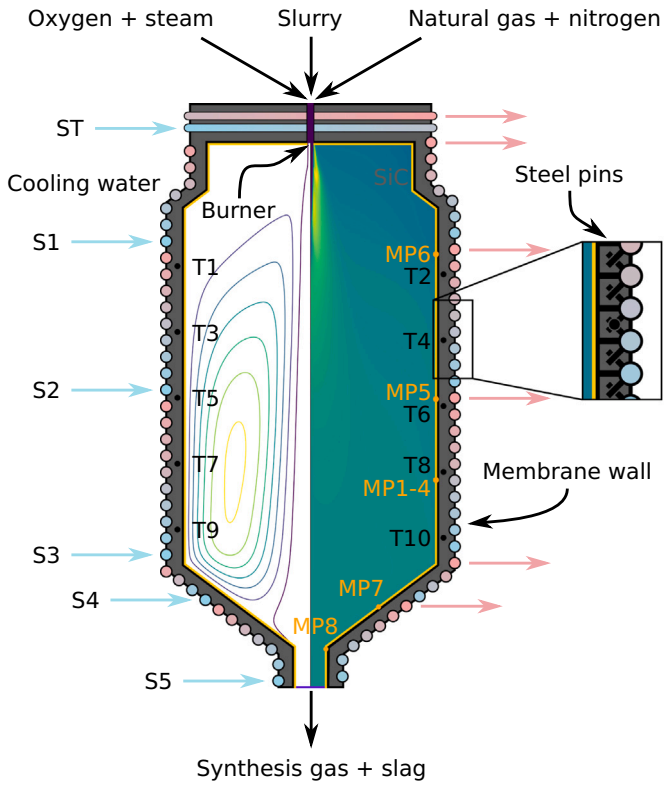

Fig. 2. Schematic cross section of the bioliq EFG reactor with the refractory thermocouples placed at positions T1, …, T10, the cooling circuits and segments S1, …, S5 and ST, and the slag measuring positions MP1-4, MP5, MP6, MP7 and MP8 [6].

pycnometry measurements, SEM analyses and X-ray diffraction (XRD) analyses.

The helium pycnometry measurements of untreated and pulverised samples were performed following DIN 66137-2:2019 [80] in order to determine whether the true solid volume and the skeletal volume are identical. Firstly, the fragment samples D-1, D-2, D-3, D-4 and D-5 with sizes between 2 mm and 15 mm (see Fig. S1) were compiled from the slag V82, collected at position D, and were analysed to determine effective densities, while accounting for unevenly distributed pores in the sample material. Secondly, the samples of slag V82, collected at positions MP6, MP5, MP1-4 and MP7, were analysed to determine effective densities; the samples were not classified into fractions of different fragment sizes due to the limited amount of sample material. Thirdly, the sample D-6 was compiled by powdering slag V82 collected at position D and was analysed to determine the true density. The measurements were conducted with the tempered measurement equipment of a helium gas-pycnometer (Quantachrome Instruments Micro-Ultrapyc 1200e MUPY-32) and weighted samples, dried at 323 K for at least 14 h and placed in the sample holder of the measurement cell. Moreover, the measurements with up to 50 runs were performed at 297 K ± 0.1 K and 19 psig (≈ 1.31 bar), where a measurement was stopped when the deviation in a set of five runs was less than 0.05%. The measurements were repeated at least five times to ensure repeatability.

The SEM analyses were carried out using the samples D-1 and D-6 of slag V82 at the Light Technology Institute of Karlsruhe Institute of Technology to identify gas enclosures. First, a fragment of sample D-1 was embedded in epoxy resin. Then, a part of the fragment and the resin were removed to obtain a cross-sectional area. The remaining part was polished with various abrasive and polishing materials. Furthermore, the powder sample D-6 was analysed without such an embedding procedure (due to the prevailing pulverised condition).

The XRD analyses were performed to determine the crystalline phases and the amorphous content of four samples: the powder sample D-6, the glass beads and pulverised samples of the slag V82 material collected at positions MP5 and MP7. The analyses were carried out using a commercial diffractometer (Malvern-PANalytical Empyrean with a multistrip PIXcel3D detector and with Cu-Kα radiation obtained using 40 kV and 40 mA) at the Institute for Technical Chemistry, Mineralogy of Karlsruhe Institute of Technology. The analyses were conducted using both pure pulverised samples and samples homogenised with 10–20% corundum standard for the quantification of the amorphous and crystalline contents. Approximately 1–2 g of each sample was pressed in a back-loaded sample holder. The samples were continuously rotated during the measurements with step sizes of 0.013° in the range between 278° and 393°. Measurement times of 399 s per step were used for the pure samples, while measurement times of 199–349 s per step were chosen for the samples with corundum standard. The phases were identified using PANalytical HighScore Plus (release 4.9) and were quantified based on Rietveld refinement using Bruker-AXS TOPAS (release 6).

3.5. Density measurements at high temperatures and surface tension measurements

The density and the surface tension of the discharged slag V82 were analysed using a sessile drop measurement setup following previous studies [7,81–83] at the Institute of Energy Materials and Devices, Structure and Function of Materials of Forschungszentrum Jülich. Firstly, pulverised samples were pressed, melted and degassed at 1573 K for 5 h under a reducing 96% argon/4% hydrogen atmosphere in graphite crucibles with an inner diameter of 5 mm. Secondly, the obtained glassy samples were heated up to a temperature of 1673 K using heating rates of 5–10 K/min under the same atmosphere. Finally, grey-scale images were recorded during the cooling and evaluated using an automated axisymmetric drop shape analysis [7]. Droplet volumes, densities and surface tensions were determined using the droplet mass and the Young–Laplace equation (for approximating the droplet contour). Further details are given in the preceding study [7].

3.6. Dynamic viscosity measurements

The dynamic viscosity of the discharged slag V82 was determined using a high-temperature viscometer (Rheotec RC1) following previous studies [14,75] at the Institute of Energy Materials and Devices, Structure and Function of Materials of Forschungszentrum Jülich. The measurements were carried out between 1173 K and 1873 K using temperature intervals of 25 K and a reducing 96% argon/4% hydrogen atmosphere [14]. Molybdenum was used for the crucibles and spindles [14]. In each single measurement, the rotational speed and the corresponding torque were varied between 1 s^{-1} and 400 s^{-1} and 0.1 mN m and 40 mN m, respectively, where measured temperatures and viscosities were affected by uncertainties of 25 K and 10%, respectively [14]. Further details are provided in previous studies [7,14,75].

3.7. Thermal conductivity measurements

The thermal conductivity of the discharged slag V82 was determined using a hot-wire measurement setup following previous studies [84–86] at the laboratory Thermal Analysis of ZAE Bayern [87]. Pt–Rh was used for the wire, and Al_2O_3 for the wire protection and the crucible. Firstly, the sample material was filled into the crucible. Secondly, several slow heating processes were carried out under an inert argon atmosphere to ensure a homogeneous degassed sample with good contact to wire and crucible, as even small gas releases can significantly affect the accuracy of the measured data. Thirdly, measurements were

conducted between 298 K and 1673 K using a heating rate of 2 K/min under an inert argon atmosphere, while stopping at up to 12 measuring points for up to 10 single measurements. After the measurements, the Al_2O_3 crucible was inspected as dissolution of Al_2O_3 was a possible risk during the measurements. The Al_2O_3 crucible, however, did not show any discolourations. Therefore, the amounts of dissolved Al_2O_3 were likely significantly smaller than the sample mass applied. Furthermore, the measured data of the single measurements were averaged for each measuring point, while the average data were smoothed using manual approximations and piecewise Gaussian filters (see Section 4.6).

3.8. Specific heat capacity measurements

The specific heat capacity of the discharged slag V82 was analysed using a differential scanning calorimeter (Netzsch DSC 404C) at the laboratory Thermal Analysis of ZAE Bayern [87]. Blank, reference and sample measurements were conducted using a Pt–Rh crucible and a heating rate of 20 K/min up to a temperature of 1673 K under an inert argon atmosphere. For the sample measurements, the crucible was first placed with 41 mg pulverised slag in a standard oven. Then, the filled crucible was heated up several times using a heating rate of 2 K/min up to a temperature of 1573 K under an inert argon atmosphere to degas the sample. After the measurements, the measured data were smoothed using manual approximations and piecewise Gaussian filters, as the sample measurements were unfortunately disturbed by heating control failures that could not be solved in this study (see Section 4.7).

3.9. Slag thickness measurements

The thickness of the slag depositions was measured at the refractory positions MP6, MP5, MP1-4 and MP7 (see Fig. 2) under ambient conditions after the bioliq EFG experiments V82, V83 and V84, i. e. the bioliq EFG reactor was shut-down after each of these experiments. The position MP6 is located in segment 2 of the bioliq EFG cooling screen (see Fig. 2), while the positions MP5 and MP1-4 are in segment 3 (see Fig. 2). At each position, some deposited and solidified slag was removed down to the refractory surface (see Fig. 14). Then, distances between refractory surface and slag surface were measured multiple times for arithmetical mean, minimum and maximum values.

3.10. Slag thickness predictions

The thickness of the slag depositions was predicted using a one-dimensional (1D) slag layer model for the segments 2 and 3 of the bioliq EFG cooling screen (see Fig. 2). This model assumes both the slag and the refractory as homogeneous layers, which is a simplification of the prevailing (complex) compositions and structures. In particular, the slag contains liquid, crystalline and solidified slag phases, while the refractory-lined membrane wall consists of (i) small steel bridges connecting the helical tubes, (ii) steel pins welded in opposite directions on the tubes and (iii) SiC filled between steel pins and bridges (see Fig. 2). However, these compositions and structures cannot be reflected in one- or even two-dimensional heat conduction models. Therefore, effective thermal conductivity approaches were employed based on an effective slag thermal conductivity λ_{slag} and an effective wall thermal conductivity λ_{wall}. The effective slag thermal conductivity λ_{slag} was described using the measured/derived data and cubic spline approximation (see Section 4.6). The effective wall thermal conductivity λ_{wall} was determined using volume fractions and thermal conductivities of both SiC and steel and employing three thermal resistance models. First, the volume fractions were derived from the geometry dimensions of the refractory-lined membrane wall, and the thermal conductivities were described using temperature dependent polynomials based on literature and manufacturer data [88,89]. Then, three thermal resistance models were combined to determine the effective wall thermal conductivity λ_{wall}: the series model, the Maxwell model and the parallel model. The series model treats SiC and steel as consecutive individual thermal resistances; the Maxwell model assumes SiC as matrix material and steel as spherical inclusions; and the parallel model is finally employed to couple the series and Maxwell resistances. Preliminary tests showed that the combination of these three thermal resistance models provides overall superior results compared to the series model, the parallel model, the geometric mean model, the Maxwell model and other combinations (see Table 9).

In addition, segmental cooling water temperatures, heat flow rates, heat transfer coefficients and gas temperatures were determined for the boundary conditions using the approaches described below:

- The segmental cooling water temperatures T_{water} were determined as means of the measured segmental cooling water temperatures at inlet and outlet [6] and are given in Table 2.
- The segmental heat flow rates $\dot{Q}$ were defined based on heat extractions derived from energy balances [6] and are listed in Table 2.
- The segmental water-side heat transfer coefficients h_{water} were estimated using latest Nusselt functions [90–92] for turbulent pipe flows and are summarised in Table 2.
- The segmental convective gas-side heat transfer coefficients $h_{conv,gas}$ were defined based on predictions of various RANS based simulations [93] following previous studies [60,72]. These CFD simulations have shown that the average (area-weighted) convective heat transfer coefficients are approximately 167 $W/(m^2K)$ for segment 2 and 302 $W/(m^2K)$ for segment 3, where the uncertainties are less than 2%.
- The segmental radiative gas-side heat transfer coefficients $h_{rad,gas}$ were determined using the segmental gas temperatures, the predicted slag surface temperatures and assumed constant slag emissivities ϵ_{slag} of 0.8 in line with the RANS based simulations [93]. The segmental radiative gas-side heat transfer coefficients $h_{rad,gas}$ are given by

$$h_{rad,gas} = \epsilon_{slag}\,\sigma\left(T_{gas}^2 + T_{slag,s}^2\right)\left(T_{gas} + T_{slag,s}\right), \tag{1}$$

  where ϵ_{slag} is the slag emissivity, σ is the Stefan–Boltzmann constant, T_{gas} is the gas temperature and $T_{slag,s}$ is the slag surface temperature.
- The segmental gas temperatures T_{gas} were defined based on predictions of various RANS based simulations [93]. These CFD simulations have provided average (area-weighted) gas temperatures that are usually about 160–210 K lower for segment 2 and 70–130 K lower for segment 3 compared to gas temperatures derived from global mass and energy balances [93]. Based on the most appropriate predictions, differences of 200 K and 115 K, respectively, were subtracted from the balanced gas temperatures $T_{bal,B}$, which are given in Table 2. Assuming rectangular distributions, the uncertainties are up to 20 K.

Finally, one-dimensional heat conduction equations were solved to determine the outer wall temperatures $T_{wall,o}$, the inner wall temperatures $T_{wall,i}$, the slag thicknesses d_{slag} and the slag surface temperatures $T_{slag,s}$ (see Fig. 3), while neglecting slag flow convection terms and source terms for chemical reactions and phase transitions. In particular, the convection terms were not accounted for because of their minor impact on the predictions for the segments 2 and 3, and source terms for crystallisation were neglected because crystallisation is likely suppressed due to the high SiO_2 contents in the glass slags [75]. The outer wall temperatures $T_{wall,o}$ and the slag surface temperatures $T_{slag,s}$ were determined by

$$T_{wall,o} = T_{water} + \frac{\dot{Q}}{A_s}\,\frac{1}{h_{water}}, \tag{2}$$

$$T_{slag,s} = T_{gas} - \frac{\dot{Q}}{A_s}\,\frac{1}{h_{conv,gas} + h_{rad,gas}}, \tag{3}$$

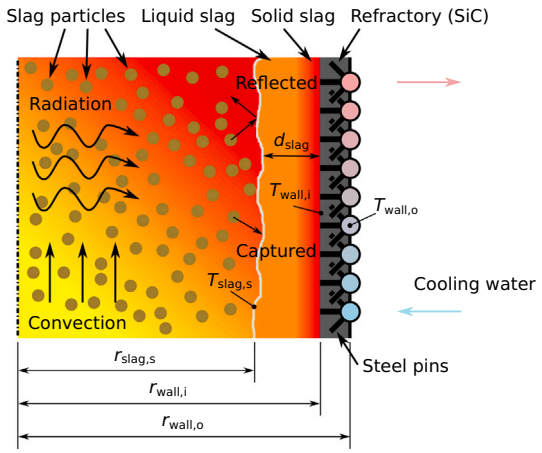

Fig. 3. Slag and wall layers.

where T_{water} is the segmental cooling water temperature, $\dot{Q}$ is the segmental heat flow rate, A_s is the segmental surface area (see [6]), h_{water} is the segmental convective water-side heat transfer coefficient, T_{gas} is the segmental gas temperature, $h_{conv,gas}$ is the segmental convective gas-side heat transfer coefficient and $h_{rad,gas}$ is the segmental radiative gas-side heat transfer coefficient. The inner wall temperatures $T_{wall,i}$ and the slag thicknesses d_{slag} were obtained using the *brentq*, *quad* and *fixed_quad* methods of SciPy [94,95] from

$$\int_{T_{wall,i}}^{T_{wall,o}} \lambda_{wall}(T)\,\mathrm{d}T = \frac{\dot{Q}}{2\pi l}\ln\left(\frac{r_{wall,o}}{r_{wall,i}}\right), \tag{4}$$

$$\int_{T_{slag,s}}^{T_{wall,i}} \lambda_{slag}(T)\,\mathrm{d}T = \frac{\dot{Q}}{2\pi l}\ln\left(\frac{r_{wall,i}}{r_{slag,s}}\right), \tag{5}$$

where λ_{wall} is the effective wall thermal conductivity, T is the temperature, l is the height of a segment, $r_{wall,o}$ is the outer wall radius, $r_{wall,i}$ is the inner wall radius, λ_{slag} is the effective slag thermal conductivity and $r_{slag,s} = r_{wall,i} - d_{slag}$ is the slag surface radius. The slag and wall temperature profiles between the characteristic temperatures were calculated using similar approaches.

4. Results

This section presents the results of the experimental slag and the experimental and numerical slag deposition analyses.

4.1. Chemical analyses

The measured oxide compositions of the glass beads and the discharged slags V82, V83, V84 and V85 in normalised mass fractions are given in Table S1. The discharged slags consisted mainly of 72–74% SiO_2, ≈ 13% Na_2O, ≈ 9% CaO and ≈ 4% MgO, while Al_2O_3, K_2O and Fe_2O_3 were found as trace components. The data also demonstrate some fluctuations in the chemical compositions of both the glass beads and the discharged glass slags. Therefore, average mass fractions were derived along with sample standard deviations from the measured and normalised compositions of each glass slag. The results are depicted in Fig. 4 and show that the fluctuations of the mass fractions are within the uncertainties. The fluctuations could thus be linked to the mineral matter variability and the analysis methods (sample selection, sample preparation, measurement equipment and measurement calibration). Moreover, the data are not sufficient to indicate mineral matter transformations, such as the vaporisation of sodium and potassium (see [75]). Therefore, average compositions can be assumed for material property predictions and other simulations. For the slag V82, an average normalised composition, accounting for Al_2O_3, CaO, K_2O, MgO, Na_2O and SiO_2, is given in Table S1. This composition was used for the model predictions in Sections 4.4–4.7.

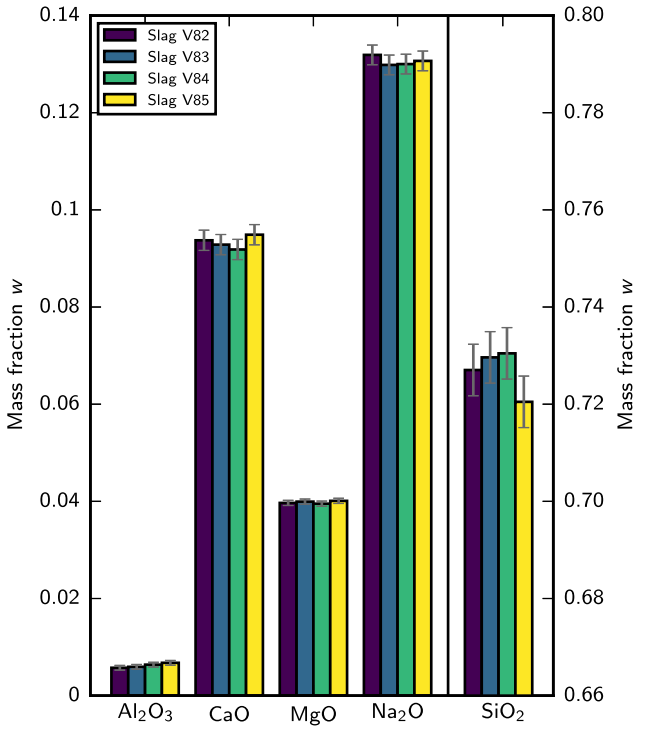

Fig. 4. Chemical compositions of slags V82, V83, V84 and V85.

Table 3
Characteristic melting temperatures of the glass beads and the discharged slags V82, V83, V84 and V85 following DIN 51730:1998 [1] (N1998) or DIN 51730:2007 [2] (N2007): average sintering temperatures T_{SST}, initial deformation temperatures T_{IDT}, softening temperatures T_{ST}, hemispherical temperatures T_{HT} and fluid temperatures T_{FT}.

Sample		Analysis	T_{SST} / K	T_{IDT} / K	T_{ST} / K	T_{HT} / K	T_{FT} / K
Glass beads	Sample 1	KIT, N1998	–	1060	1110	1210	1400
	Sample 2	Eurofins, N2007	1000	1080	1170	1340	1480
Slag V82	Sample 1	KIT, N1998	950	1050	1110	1290	1420
	Sample 2	KIT, N1998	960	1070	1110	1290	1430
Slag V83	Sample 1	KIT, N1998	900	1060	1210	1290	1420
	Sample 2	KIT, N1998	900	1050	1220	1290	1420
Slag V84	Sample 1	KIT, N1998	960	1060	1110	1290	1410
	Sample 2	KIT, N1998	960	1060	1110	1300	1420
Slag V85	Sample 1	KIT, N1998	880	1040	1080	1260	1420
	Sample 2	KIT, N1998	880	1040	1090	1290	1430

4.2. Melting analyses

The measured characteristic melting temperatures of the glass beads and the discharged slags V82, V83, V84 and V85 are listed in Table 3. The data demonstrate some fluctuating sintering, hemispherical and fusion temperatures for the glass beads as well as similar initial deformation temperatures, hemispherical and fusion temperatures for the discharged slags. In addition, the slags V82 and V84 have shown similar sintering temperatures and softening temperatures, while lower sintering temperatures and deviating softening temperatures have been found for the discharged slags V83 and V85. These findings do not match the different compositions of the glass beads and the slags V82, V83, V84 and V85 and suggest that the fluctuations in the compositions and melting temperatures should not be overrated, as they could primarily be

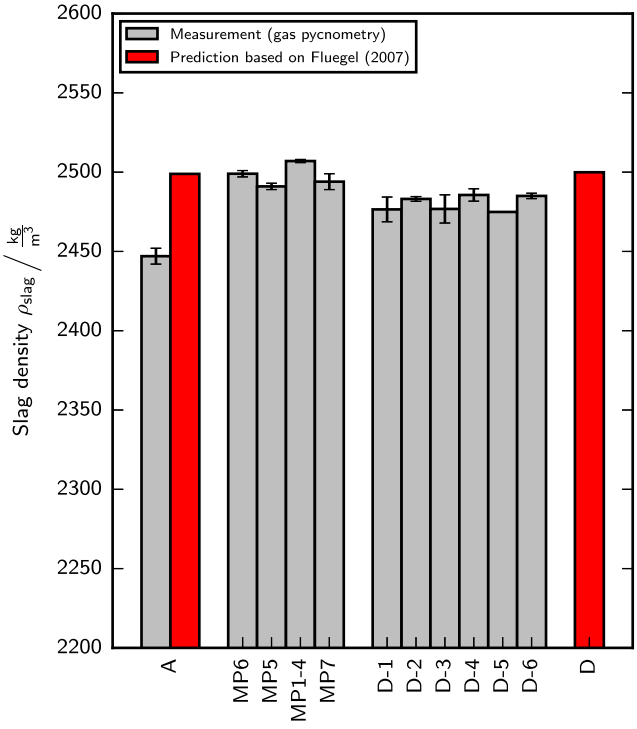

Fig. 5. Density ρ_{slag} of slag V82 under ambient conditions. A: measured and predicted densities of the glass beads; MP6, MP5, MP1-4, MP7: measured densities of slag V82 samples collected at positions MP6, MP5, MP1-4 and MP7; D-1, D-2, D-3, D-4, D-5, D-6: measured densities of slag V82 samples collected at position D; D: predicted density of slag V82 for position D.

Table 4
Densities of the glass beads and the slag V82 samples under ambient conditions based on helium pycnometry measurements. The uncertainties were calculated as standard deviation of the measurement results in the case of the glass beads or as standard deviation of the sample results in the other cases.

Sample	$\frac{\rho_{slag}}{kg/m^3}$
Glass beads	2447 ± 5
Mean based on slag samples collected at positions D-1, …, D-6	2481 ± 3
Mean based on slag samples collected at positions MP1-4, …, MP7	2498 ± 6

linked to the mineral matter variability and the analysis methods (see Section 4.1). Furthermore, the deviating melting behaviour of the glass beads might be connected with different densification behaviour between 900 K and 1100 K and the solution of CO_2 and H_2O in slag at pressurised conditions.

4.3. Density measurements at ambient temperatures and morphology analyses

The densities measured under ambient conditions are shown in Fig. 5 and are listed in Table 4. The densities of the discharged slag V82 samples D-1, …, D-6 are similar despite different sizes and shapes, where the average slag density is $2481\,kg/m^3 \pm 3\,kg/m^3$. In particular, the density of the powder sample D-6 does not significantly deviate from the densities of the fragment samples D-1, …, D-5. Assuming that helium did not significantly penetrate into the fragment samples D-1, …, D-5 and that the enclosed pores of the powder sample D-6 were destroyed through grinding, the solidified slags have contained only tiny amounts of physically enclosed gas. Following DIN 66137-2:2019 [80], the true solid volume and the skeletal volume have been almost identical. To

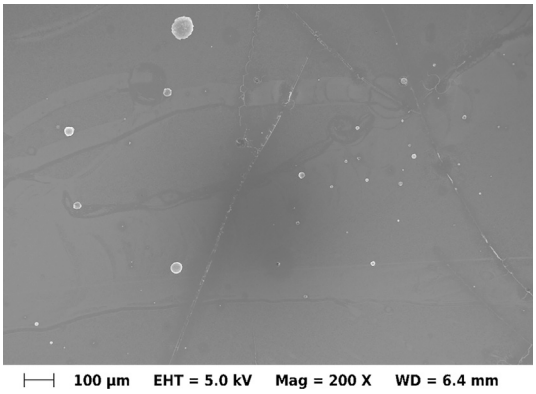

Fig. 6. SEM image of a cross-section of a fragment from the slag V82 sample D-1.

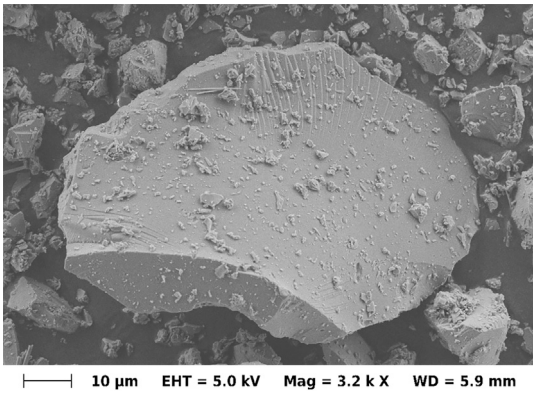

Fig. 7. SEM image of a particle from the slag V82 sample D-6.

confirm this finding, however, the samples D-1 and D-6 were further analysed using SEM analyses.

The cross-section of a fragment of sample D-1 is shown in Fig. 6. The cross-section has an area porosity significantly smaller than 1% and exhibits a few pores of different sizes below 80 µm only. These pores are not filled with embedding material and were thus not accessible in the original fragment. Therefore, these pores can be identified as enclosed pores. Furthermore, the surface of a particle found in the pulverised sample D-6 is shown in Fig. 7. The surface does not exhibit any pores as most particle diameters were smaller than 80 µm. Moreover, the marks of the grinding procedure are clearly visible on the particle surface. This indicates that the powder was not suitable to identify small enclosed pores below 10 µm due to the mechanical stress of grinding. Overall, however, the SEM analyses confirm that the discharged slags have not exhibited larger amounts of pore volumes.

Furthermore, the measured densities of the slag samples collected at positions MP6, MP5, MP1-4 and MP7 after the bioliq EFG experiment V82 are shown in Fig. 5 and are listed in Table 4. The cooling screen samples have thus exhibited similar densities, which, however, are larger than the densities measured for the samples D-1, …, D-6 and the glass beads. These deviations cannot be explained by slightly different oxide compositions (for example, based on the ambient-temperature density model of Fluegel [96] for glasses). Therefore, the powder sample D-6, the glass beads and two pulverised samples (based on the samples collected at the positions MP5 and MP7) were examined using XRD analyses in order to find out whether the smaller densities of the glass beads and the samples D-1, …, D-6 were due to higher cooling and solidification rates.

The diffractograms of the pure samples (without corundum standard) are shown in Fig. S2 and reveal that the samples analysed consisted mainly of amorphous glass (98.3–99.9%). In addition, the sample collected at position MP5 also contained wollastonite (1.1%), cristobalite (0.2%) and tridymite (0.3%), while the sample collected at position MP7 included small amounts of cristobalite (0.2%) and tridymite (0.09%). Furthermore, small amounts of Na_2CaSiO_4 (0.06%) and crystalline quartz (below 0.1%) were found in the slag sample D-6 and in the glass beads and cooling screen samples, respectively. The samples analysed have thus contained only small amounts of crystalline phases. In particular, the glass beads and the sample D-6 did not consist of different or less crystalline structures compared to the cooling screen samples collected at positions MP5 and MP7. Therefore, the crystalline structures have not caused the lower densities of the samples D-1, …, D-6, while slag drain did not significantly affect the slag densities in agreement with previous findings [14,75].

4.4. Density measurements at high temperatures and surface tension measurements

The measured slag surface tensions of the discharged slag V82 are shown in Fig. 8 and have been approximated by

$$\gamma_{\mathrm{slag}} = \left(2.65476 \cdot 10^{2} + 1.33202 \cdot 10^{-1} \exp\left(4.09170 \cdot 10^{-3} \frac{T}{\mathrm{K}}\right)\right) \frac{\mathrm{mN}}{\mathrm{m}}, \quad (6)$$

where γ_{slag} is the surface tension of the liquid slag and T is the temperature. The measured data are between 275 mN/m at 1173 K and 410 mN/m at 1673 K and exhibit only a few outliers. Previous models [97–100], however, predict values between 316 mN/m and 333 mN/m at 1673 K for the model slag. In addition, Kucuk et al. [100] measured 306 mN/m ± 5 mN/m at 1673 K for a similar soda–lime–silica melt (15% Na_2O–10% CaO–75% SiO_2). This indicates measurement uncertainties of approximately 20%. Following previous internal measurements (which only exhibited uncertainties of 5–10%), the uncertainties are primarily linked to droplet contour approximations (e. g. due to non-escaped gas bubbles).

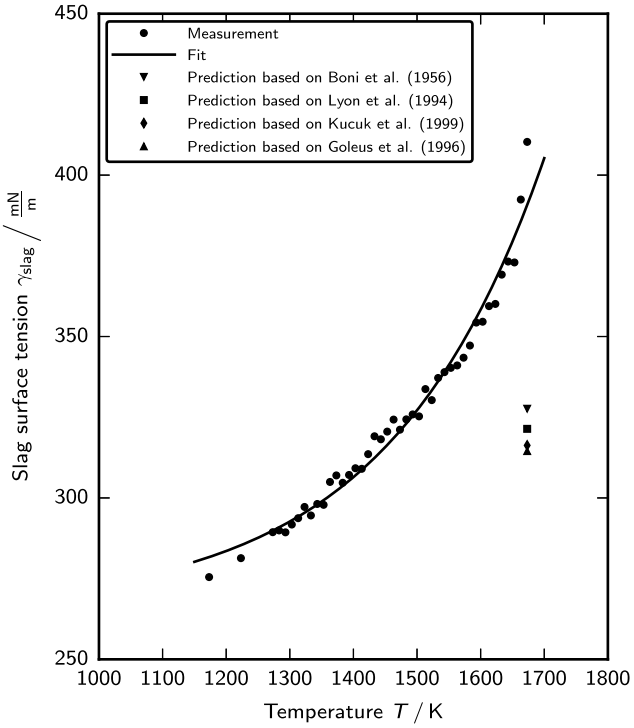

Fig. 8. Surface tension γ_{slag} of slag V82.

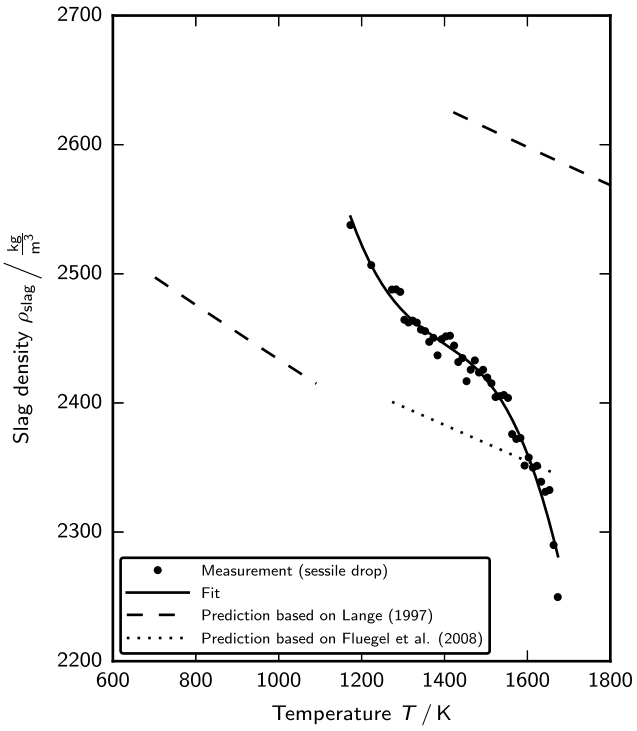

Fig. 9. Density ρ_{slag} of slag V82.

The measured densities of the discharged slag V82 are shown in Fig. 9 and have been approximated by

$$\rho_{\mathrm{slag}} = \left(1.55230 \cdot 10^{4} - 2.77484 \cdot 10^{1} \left(\frac{T}{\mathrm{K}}\right) + 1.97785 \cdot 10^{-2} \left(\frac{T}{\mathrm{K}}\right)^{2} - 4.73592 \cdot 10^{-6} \left(\frac{T}{\mathrm{K}}\right)^{3}\right) \frac{\mathrm{kg}}{\mathrm{m}^3}, \quad (7)$$

where ρ_{slag} is the density of the liquid slag and T is the temperature. The measured data vary between 2250 kg/m^3 and 2538 kg/m^3 and are mainly between the predictions of the models of Lange [101] and Fluegel et al. [102]. The measured data might therefore have uncertainties of approximately 5%, which are also connected with the droplet contour approximations (see above).

4.5. Dynamic viscosity measurements

The measured dynamic viscosities of the discharged slag V82 are shown in Fig. 10 and have been approximated by

$$\eta_{\mathrm{slag}} = 6.18467 \cdot 10^{-6} \exp\left(\frac{2.39510 \cdot 10^{4}}{T/\mathrm{K}}\right) \mathrm{Pa\,s}, \quad (8)$$

where η_{slag} is the dynamic viscosity of the liquid slag and T is the temperature. The measured data reflect the glassy nature of slag V82 and are in good agreement with the predictions based on the structure-based model of Wu et al. [103–107], which has been developed for both the liquid phase and the supercooled phase below the liquidus temperature.

4.6. Thermal conductivity measurements

The measured thermal conductivities of the discharged slag V82 are shown with uncertainty bars in Fig. 11. The uncertainty bars were defined using the uncertainties of the temperature and thermal conductivity measurements employed; the thermal conductivity measurements have typically exhibited relative uncertainties of approximately 5%. The measured slag thermal conductivities are mainly in good agreement with

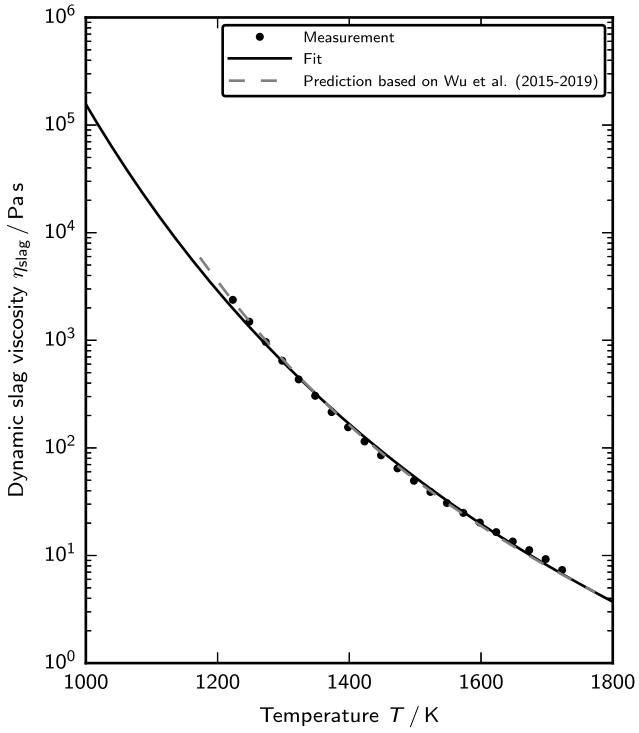

Fig. 10. Dynamic viscosity η_{slag} of slag V82.

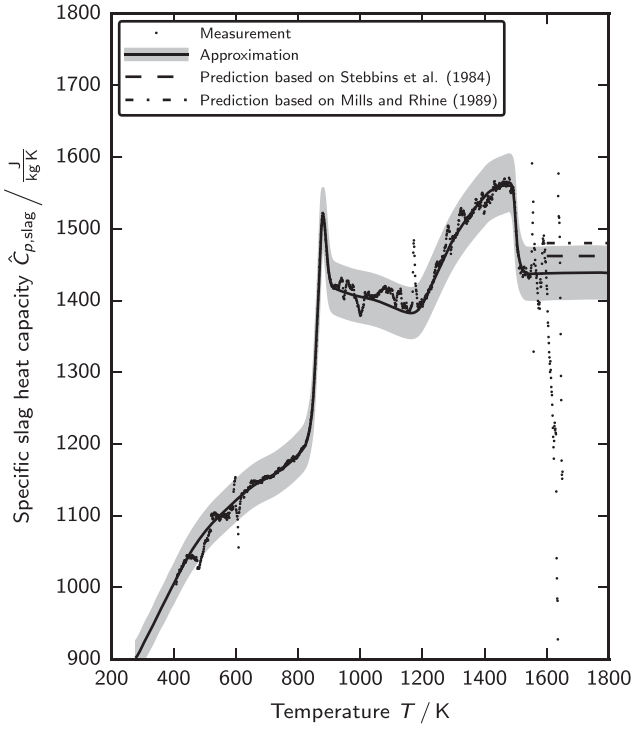

Fig. 12. Specific heat capacity $\hat{C}_{p,slag}$ of slag V82.

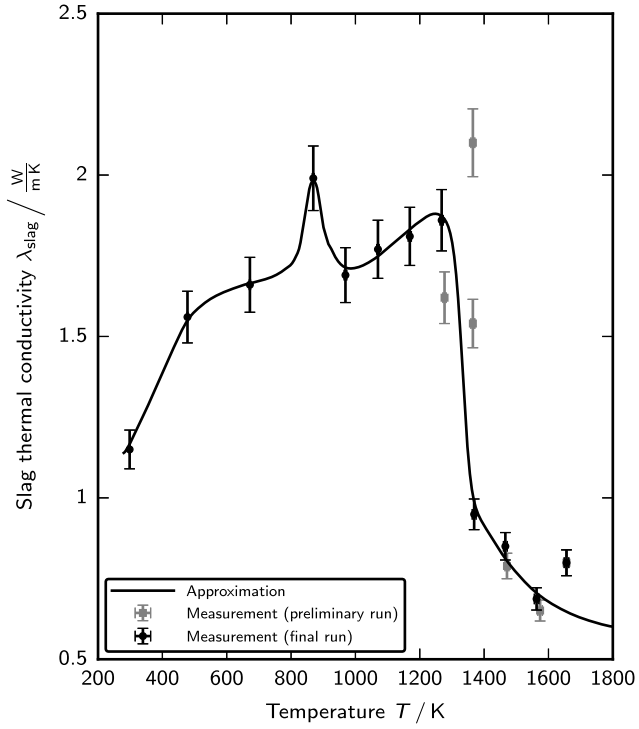

Fig. 11. Thermal conductivity λ_{slag} of slag V82.

previous data [108,109] of two glass melts with similar compositions (10% Na_2O–20% CaO–70% SiO_2 and 20% Na_2O–10% CaO–70% SiO_2). However, previous measurement data do not exhibit any peaks at glass transition and decrease to approximately 0.2 W/(m K) between 1200 K and 1800 K. This could be because of the impact of the composition, as small changes in CaO and Na_2O contents significantly affect the thermal conductivity [108,109]. Furthermore, the measured data are in good agreement with (i) the model of Choudhary and Potter [110], which predicts 1.33 W/(m K) ± 0.13 W/(m K) for ambient conditions, (ii) a manufacturer's data sheet [111], which reports 1.5 W/(m K) at 773 K for glass beads similar to the Arteka glass beads, and (iii) data of a preliminary measurement, which are also shown in Fig. 11. Therefore, the measured data are reliable within the measurement uncertainties and were approximated using manual and numerical approaches at a root mean squared deviation of 0.05 W/(m K). The derived data are tabulated in the Supplementary material and can be incorporated using cubic spline interpolation.

4.7. Specific heat capacity measurements

The measured specific heat capacities of the discharged slag V82 are shown together with a grey shaded ±2.5% uncertainty range in Fig. 12. The measured data are strongly disturbed by heating control failures (see Section 3.8). Therefore, the peaks and fluctuations between 500 K and 700 K and between 900 K and 1200 K and the interferences above 1550 K were discarded for the approximation. Moreover, the measured data reflect the glass transition between 820 K and 900 K and show a decreasing trend after the glass transition followed by an increasing trend above 1170 K. The latter observations differ from previous findings for biomass slags, where the specific heat capacity has increased with increasing temperature between 1023 K and 1273 K [7]. However, this could be related to the different compositions. The trends might also be connected with partial recrystallisation and remelting processes, which would be in accordance with the fluid temperatures of 1420–1430 K (see Table 3). Above 1490 K, the measured data decrease again to 1439 J/(kg K) and might then be assumed to be constant. This is in agreement with previous models [68,112], which predict values between 1462 J/(kg K) and 1480 J/(kg K) for the average composition of the model slag. Therefore, the measured data are reliable within the uncertainties and were approximated using manual and numerical approaches at a root mean squared deviation of 12.3 J/(kg K) below 1460 K. The derived specific heat capacities are tabulated in the Supplementary material and can be incorporated using cubic spline interpolation.

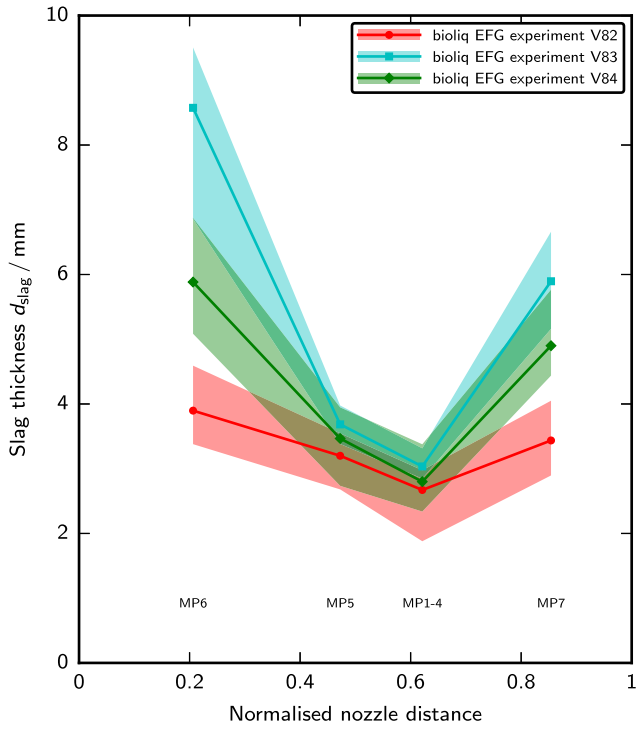

Fig. 13. Slag thickness d_{slag} measured at positions MP6, MP5, MP1-4 and MP7 after reactor shut-down.

4.8. Slag thickness measurements

The slag thicknesses measured after the bioliq EFG experiments V82, V83 and V84 are shown in Fig. 13 and are given in Tables 5–8. First of all, the measured data exhibit large fluctuations. This is in agreement with previous measurements [7,51] and reflects the non-uniform slag depositions that were observed during visual inspections and are shown in Fig. 14. The large uncertainties might also be linked to burst bubbles, which were present due to the release of gases during solidification (see Section 5.1.3), even though the bubbles were ignored as far as possible when conducting the measurements. Moreover, the measured data suggest that the slag deposition is the thickest at the uppermost position (MP6). This contradicts previous measurement data [7,51], which indicated mainly an increase in slag thickness from the top to the gasifier outlet. The measured data also suggest that the slag deposition was mainly thicker after the bioliq EFG experiment V83 than after the bioliq EFG experiments V82 and V84. However, twice the amount of glass beads was supplied in the bioliq EFG experiment V84, while similar amounts of glass beads were used in the bioliq EFG experiments V82 and V83 at similar (balanced) gas temperatures (see Table 2). Both deviations could be linked to (i) transient effects during reactor shut-down and (ii) non-quasi-stationary conditions of the slag flow during operation (see Section 5.3.2). Therefore, the measured slag thicknesses should be examined and verified using numerical approaches (see Section 4.9), while future studies may develop experimental online methods for determining superior data under process conditions and over longer operating times to ensure stationary conditions in both gas and slag phases.

4.9. Slag thickness predictions

The slag thicknesses were predicted using the 1D slag layer model and the derived thermal conductivity data (see Section 4.6). The results are shown for the bioliq EFG experiments V82, V83 and V84 and the segments 2 and 3 in Figs. 15–17, where the uncertainty bars are based on estimated uncertainties in the assumed gas temperatures (see Section 3.10). The predictions are compared with both experimental

Table 5
Mean slag thicknesses $d_{slag,exp,mean}$, minimum slag thicknesses $d_{slag,exp,min}$ and maximum slag thicknesses $d_{slag,exp,max}$ measured at position MP6 after reactor shut-down.

Experiment	$d_{slag,exp,mean}$ / mm	$d_{slag,exp,min}$ / mm	$d_{slag,exp,max}$ / mm
V82	3.9	3.0	5.1
V83	8.6	5.6	10.2
V84	5.9	4.5	7.6

Table 6
Mean slag thicknesses $d_{slag,exp,mean}$, minimum slag thicknesses $d_{slag,exp,min}$ and maximum slag thicknesses $d_{slag,exp,max}$ measured at position MP5 after reactor shut-down.

Experiment	$d_{slag,exp,mean}$ / mm	$d_{slag,exp,min}$ / mm	$d_{slag,exp,max}$ / mm
V82	3.2	2.3	3.8
V83	3.7	3.2	4.2
V84	3.5	2.2	4.3

Table 7
Mean slag thicknesses $d_{slag,exp,mean}$, minimum slag thicknesses $d_{slag,exp,min}$ and maximum slag thicknesses $d_{slag,exp,max}$ measured at position MP1-4 after reactor shut-down.

Experiment	$d_{slag,exp,mean}$ / mm	$d_{slag,exp,min}$ / mm	$d_{slag,exp,max}$ / mm
V82	2.7	1.3	3.2
V83	3.0	2.7	3.5
V84	2.8	2.0	3.8

Table 8
Mean slag thicknesses $d_{slag,exp,mean}$, minimum slag thicknesses $d_{slag,exp,min}$ and maximum slag thicknesses $d_{slag,exp,max}$ measured at position MP7 after reactor shut-down.

Experiment	$d_{slag,exp,mean}$ / mm	$d_{slag,exp,min}$ / mm	$d_{slag,exp,max}$ / mm
V82	3.4	2.5	4.5
V83	5.9	4.6	7.2
V84	4.9	4.1	6.4

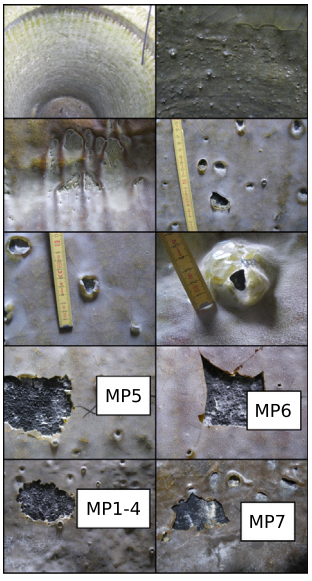

Fig. 14. Images of the solidified slag depositions after the bioliq EFG experiments V82, V83 and V84.

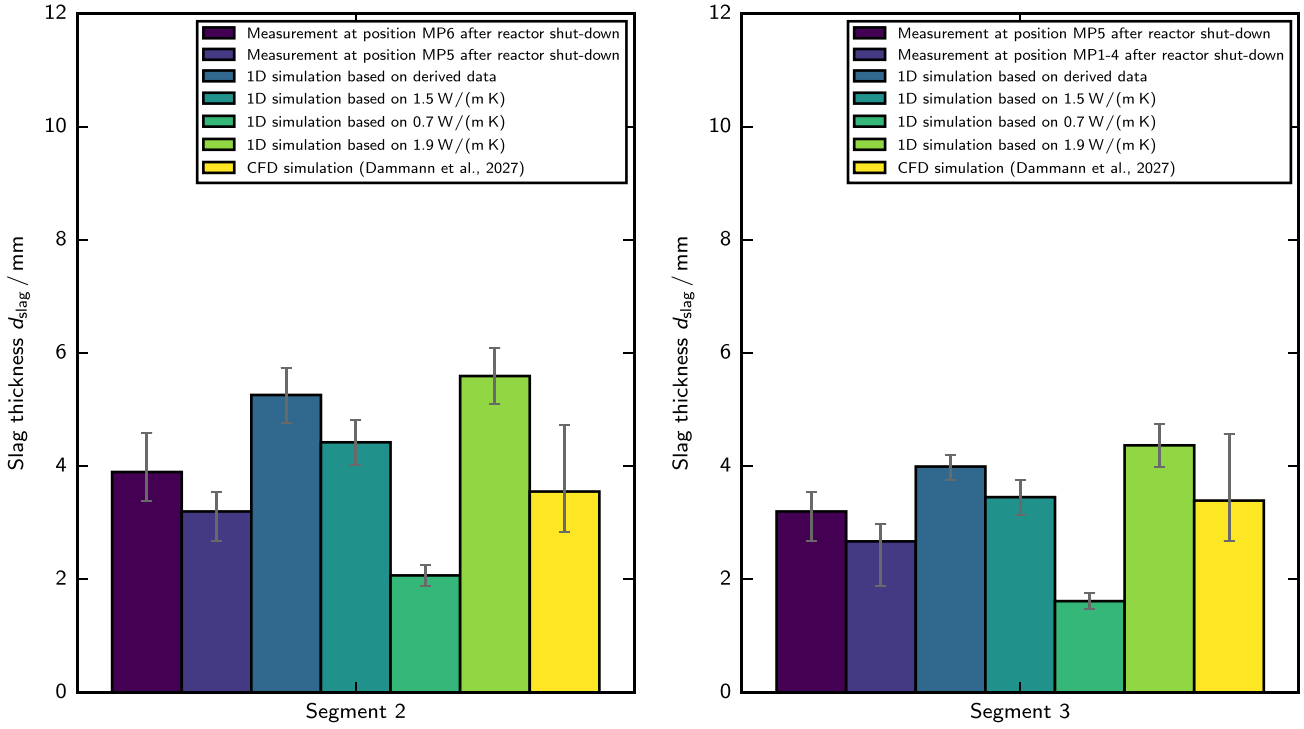

Fig. 15. Measured and predicted slag thicknesses d_{slag} for the bioliq EFG experiment V82.

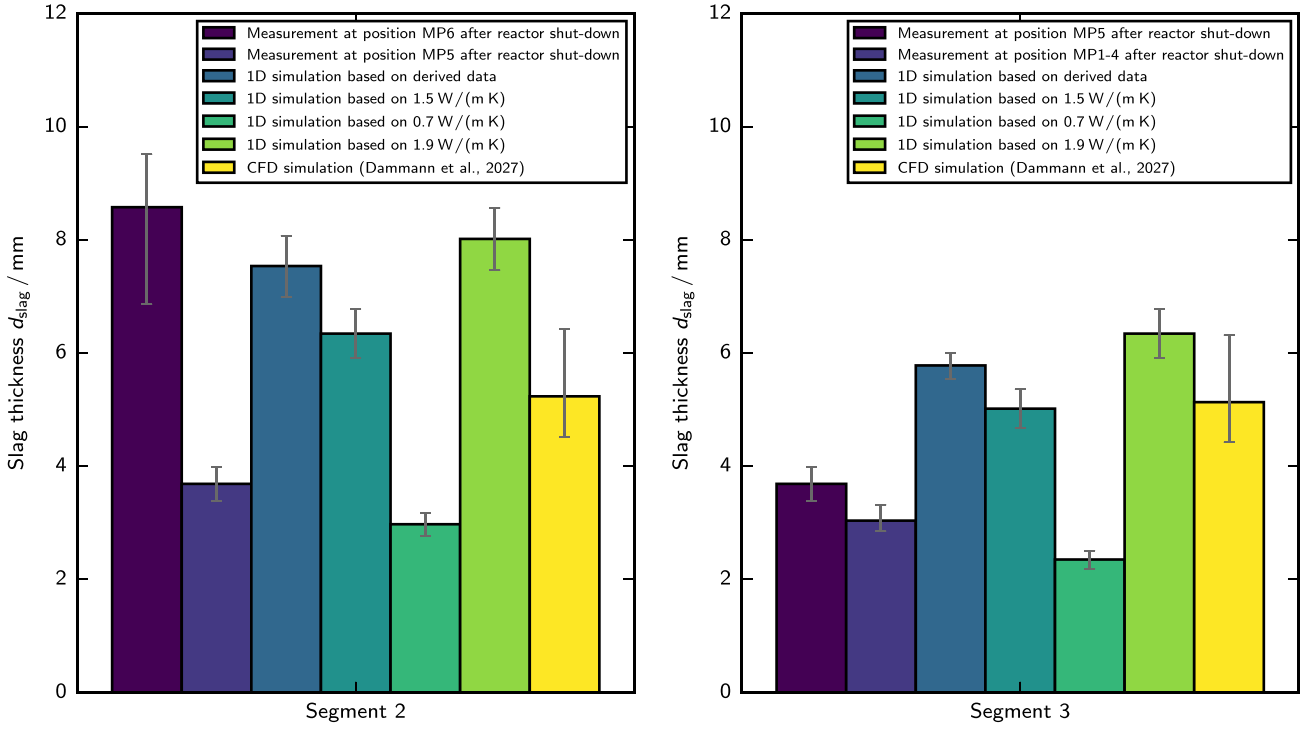

Fig. 16. Measured and predicted slag thicknesses d_{slag} for the bioliq EFG experiment V83.

and CFD data. The experimental data were derived from the measurements at positions MP6, MP5 and MP1-4. The data determined for position MP5 are shown for both segments, as MP5 is located at the top of segment 3 and just below segment 2. The uncertainties in the experimental data were obtained from the minimum and maximum values assuming rectangular distributions. The CFD data, in turn, were determined using various RANS based simulations [93] following previous studies [60,72]. The uncertainties in these predictions are about +1.2 mm and −0.7 mm (assuming again rectangular distributions) and are quite large because of various modelling assumptions and simplifications for inlet conditions, turbulence-chemistry interactions, homogeneous kinetics, particle dispersion and slag flow [93]. For example, the turbulence modelling strongly determines the particle dispersion in the boundary layer and thus the local slag deposition.

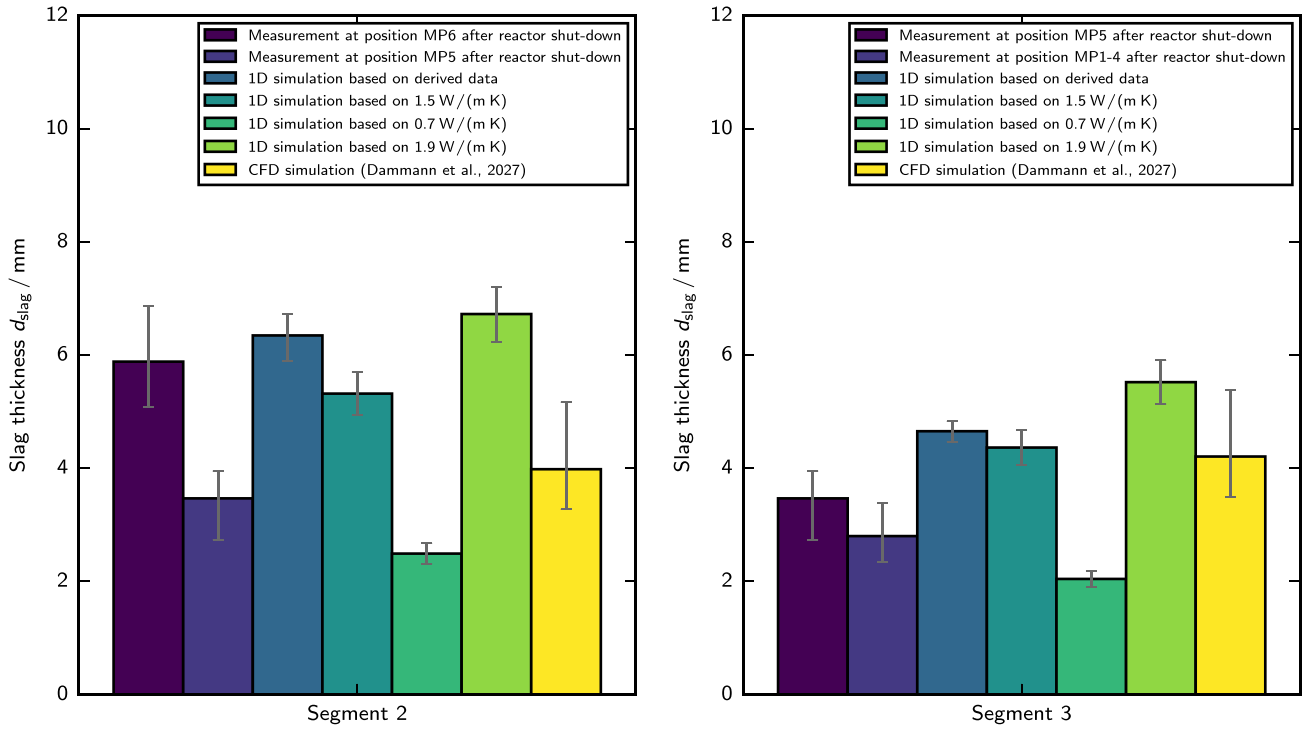

Fig. 17. Measured and predicted slag thicknesses d_{slag} for the bioliq EFG experiment V84.

The comparisons show that the predictions are only in good to fair agreement with the measurements. This is because of (i) non-uniform SiC coating, (ii) non-uniform slag deposition (see Section 4.8), (iii) transient slag flow effects and (iv) model assumptions and simplifications. In addition, the predictions are in better agreement with the experimental data for segment 2 than with the data for segment 3 and are mainly in better agreement with the data for the upper measuring position (MP6 for segment 2 and MP5 for segment 3) than with the data for the lower measuring position (MP5 for segment 2 and MP1-4 for segment 3). This indicates that the slag thickness data measured under ambient conditions after reactor shut-down could underestimate the thickness of the slag depositions in the experiments (see Section 4.8). Therefore, such (imperfect) data should be examined using appropriate slag layer models, before employing the data for validating CFD models.

Furthermore, the predictions of the 1D simulations are mainly in good agreement with the predictions of the CFD simulations but also show the impact of the gas temperature on the predictions. Specifically, the uncertainties in the predictions (based on the assumed gas temperature uncertainty) are larger for segment 2 than for segment 3. This is linked to the temperature dependence of the slag thermal conductivity data and demonstrates that assumptions of one-dimensional slag layer simulations can strongly alter the predictions (see Sections 5.2.1–5.2.3 and Section 5.2.6). Therefore, such simulations should always be coupled with CFD simulations to derive appropriate boundary conditions and to provide consistent predictions.

5. Discussion

This section discusses the analyses and measurements, the predictions and possible applications of the derived slag property and slag layer models.

5.1. Analyses and measurements

This section discusses the influences of the atmospheric measuring conditions and the gas atmospheres on the measured data as well as the findings regarding the gas enclosures.

5.1.1. Atmospheric measuring conditions

The samples solidified under pressurised conditions, whereas the analyses and measurements were conducted under atmospheric pressures in line with previous studies [7,14,48] and in the absence of measuring devices for elevated pressures. When melting the samples under atmospheric pressures, gases are released and can interfere with analyses and measurements. Therefore, the gases were removed from the samples, and the analyses and measurements were repeated multiple times. However, the removal of chemically dissolved gases (e. g. CO_2 and H_2O) changes the chemical composition and may affect the slag properties [113]. For example, the dynamic viscosity increases with increasing H_2O content and likely decreases with increasing CO_2 content. However, the quantitative influences of chemically bound gases on the chemical and physical properties are unknown and may be investigated in future works.

5.1.2. Gas atmospheres

The measurements of dynamics viscosity, (high-temperature) density and surface tension were conducted under reducing argon–hydrogen atmospheres, whereas those of thermal conductivity and specific heat capacity were done under inert argon gas because hydrogen containing gases could not be used in the respective measuring devices. Such non-reducing atmospheres can have a significant effect on slag properties when the slag consists of large quantities of oxides with different oxidation states. However, the slag V82 contains much less than 1% Fe_2O_3 (see Table S1). Therefore, the use of argon atmospheres had a minor impact on the measured data.

5.1.3. Gas enclosures

The visual inspections after the bioliq EFG experiments showed numerous burst gas bubbles in the solidified slag deposition (see Section 4.8). Such bubbles as well as porous structures of solidified slag have been connected with gas formed due to reactions of captured carbon or refractory material, where the gas is trapped in the slag layers because of the continuous slag deposition and flow [50,79].

Table 9
Relative deviations of slag thickness d_{slag} from baseline predictions: impact of the wall thermal conductivity λ_{wall}, the slag thermal conductivity λ_{slag}, the gas temperature T_{gas}, the convective gas-side heat transfer coefficient $h_{conv,gas}$ and the slag emissivity ϵ_{slag}.

Case	Relative deviations of slag thickness d_{slag} from baseline predictions /%					
	V82		V83		V84	
	Segment 2	Segment 3	Segment 2	Segment 3	Segment 2	Segment 3
λ_{wall} based on Maxwell model	+13.2	+15.3	+10.5	+10.8	+10.9	+13.2
λ_{wall} based on geometric mean model	+54.0	+60.9	+38.3	+45.6	+44.6	+52.6
λ_{wall} based on series model	−15.1	−17.5	−11.4	−12.3	−12.5	−15.1
λ_{wall} based on parallel model	+59.7	+70.8	+42.0	+52.4	+49.3	+61.1
λ_{wall} = 8.7 W/(m K)	−5.9	+0.8	−4.1	+1.4	−4.8	+0.8
λ_{wall} = 8.25 W/(m K)	−14.3	−11.1	−10.1	−6.6	−11.8	−9.3
λ_{wall} = 9.15 W/(m K)	+1.8	+11.4	+1.6	+8.5	+1.5	+9.9
λ_{slag} ·= 0.95	−5.0	−5.0	−5.0	−5.0	−5.0	−5.0
λ_{slag} ·= 1.05	+5.0	+5.0	+5.0	+5.0	+5.0	+5.0
λ_{slag} = 1.5 W/(m K)	−15.9	−13.5	−15.9	−13.2	−16.2	−6.2
λ_{slag} = 0.7 W/(m K)	−60.6	−59.6	−60.6	−59.4	−60.8	−56.1
λ_{slag} = 1.9 W/(m K)	+6.4	+9.4	+6.4	+9.7	+6.0	+18.6
T_{gas} −= 20 K	−9.4	−5.7	−7.3	−4.3	−7.1	−3.9
T_{gas} += 20 K	+9.2	+4.9	+7.1	+3.7	+5.9	+3.7
$T_{gas} = T_{gas,CFD}$	+7.0	+4.1	−3.0	−3.2	−0.5	−0.2
$T_{gas} = T_{WGS,B}$	+39.5	+7.6	+33.5	+9.6	+28.2	+11.4
$h_{conv,gas}$ ·= 0.97	−0.6	−0.4	−0.4	−0.2	−0.3	−0.2
$h_{conv,gas}$ ·= 1.03	+0.6	+0.3	+0.4	+0.2	+0.3	+0.2
ϵ_{slag} = 0.6	−15.1	−7.2	−10.3	−4.7	−11.3	−4.7
ϵ_{slag} = 0.4	−38.9	−22.5	−26.6	−14.4	−30.6	−12.4

Moreover, the analysis and measurement preparations of this study indicated the release of significant amounts of gas when melting the samples. However, the density measurements at ambient temperatures and the morphology analyses showed only tiny amounts of physical gas enclosures (see Section 4.3) in contrast to previous findings [50]. In addition, the ultimate analyses of the slag samples in the preceding study [6] demonstrated low carbon contents[1]. Therefore, the burst gas bubbles cannot be linked only to chemical reactions and physical gas enclosures; they could rather be the result of various effects. Some gas might have been formed due to reactions of captured soot and then been trapped due to the continuous slagging process. This gas could also tend to diffuse out of the molten slag. Other gas has been chemically dissolved, as the gas solubility increases with increasing pressure, and may have been released due to local temperature, pressure and velocity fluctuations, which are particularly strong during reactor shut-down. Finally, the sizes of burst gas bubbles might have resulted in an overestimation of enclosed gas. High-temperature endoscopy in combination with high-speed photography [114] may be used to monitor the local slag flow in future slagging experiments.

5.2. Predictions

This section analyses the slag layer model sensitivities and the predicted profiles of slag thermal conductivity, slag velocity, and slag and wall temperatures.

5.2.1. Impact of wall thermal conductivity

The wall thermal conductivity λ_{wall} was described using thermal resistance models, whereas constant values may be sufficient considering the complex wall structures and the simplified modelling approach. Therefore, additional 1D simulations were carried out using three values: 8.25 W/(m K), 8.7 W/(m K) and 9.15 W/(m K). Relative deviations from the baseline predictions are compared in Table 9. The results show that an average wall thermal conductivity of 8.7 W/(m K) provides similar predictions as the thermal resistance approach. Moreover, the predicted slag thickness changes up to 14% when the average wall thermal conductivity is altered by about 5%. Therefore, both 1D and CFD simulations should describe the wall thermal conductivity using appropriately adjusted wall thermal conductivity data (see Section 5.2.6).

5.2.2. Impact of slag thermal conductivity

The slag thermal conductivity λ_{slag} was described using the derived temperature-dependent data, which exhibits uncertainties of ±5%. In addition, constant values were used in most previous studies due to lack of data (for example, see [51,60]). Therefore, additional 1D simulations were conducted using the derived data altered by ±5% and using three constant values: 0.7 W/(m K), 1.5 W/(m K), 1.9 W/(m K). These values represent minimum, mean and maximum values of the derived thermal conductivity data (see Section 4.6). The predicted slag thicknesses are shown in Figs. 15–17, while relative deviations from the baseline predictions are listed in Table 9. The comparisons show that the predicted slag thickness changes by about 5% when the derived slag thermal conductivity data are increased or decreased by 5%. In contrast, larger deviations are found for the 1D simulations based on constant values. For 1.5 W/(m K) and 1.9 W/(m K), the predicted slag thickness changes between −16% and 19%, while the predictions are mainly in good to fair agreement with the predictions that were obtained using the derived data. This indicates average slag thermal conductivities of about 1.7 W/(m K). For 0.7 W/(m K), the deviations are between −56% and −61%, while the predicted values are mainly close to the measured data for segment 3. The deviations between predicted and measured data can therefore be reduced by assuming lower slag thermal conductivities in line with previous assumptions [51]. However, this would not reflect the measured thermal conductivity data and the small amount of physical gas enclosures and contradict the results for segment 2 and the bioliq EFG experiments V83 and V84. In summary, the prediction of the slag thickness strongly depends on the slag thermal conductivity data. Therefore, both 1D and CFD simulations should be based on appropriate (measured) thermal conductivity data rather than on guessed data.

5.2.3. Impact of gas boundary conditions

The gas boundary conditions were defined based on various CFD predictions (see Section 3.10). These predictions, however, are affected by modelling uncertainties (see Section 4.9) and are typically not available for a wide range of operating and process conditions. Therefore,

[1] The carbon content of slags V82, V83 and V84 was less than 0.1% (i. e. below the detection limit), whereas the carbon content of slag V85 was 0.4% [6].

sensitivity analyses were conducted to investigate the impact of the gas boundary conditions on the slag thickness predictions. The relative deviations from the baseline predictions are presented in Table 9, while the findings are summarised below:

1. The slag thickness only slightly changes if the gas temperatures are defined based on the average gas temperatures that have been obtained from the CFD simulations. Therefore, the assumed gas temperatures have been good guesses for the boundary conditions of the baseline simulations.
2. The slag thickness strongly increases for segment 2 and changes less for segment 3 if the gas temperatures are described using the WGS temperatures at position B $T_{WGS,B}$[2]. This is because the average gas temperatures of segment 3 are close to the WGS temperatures and those of segment 2 are usually 100–200 K lower than the WGS temperatures.
3. The convective gas-side heat transfer coefficient only slightly affects the predictions. Therefore, for 1D simulations, this coefficient can be assumed based on previous CFD simulations for similar process conditions.
4. The slag emissivity significantly affects the predictions of the slag thickness, which decreases with reduced slag emissivity at constant heat extraction. Therefore, for both 1D and CFD simulations, the slag emissivity should be based on experimental data.

In summary, the accuracy of the gas temperature and the slag emissivity is crucial for the prediction of the slag thickness, while the accuracy of the convective gas-side heat transfer coefficient is less important for that.

The results also show that the deviations between measured and predicted data can be reduced by assuming higher gas temperatures or lower slag emissivities. However, analyses [6,93] have shown that, in the lower reactor part, the WGS temperature is close to the gas temperature for the bioliq EFG experiments V82, V83 and V84. Therefore, the deviations between measured and predicted slag thicknesses cannot be linked to erroneous gas temperatures but are rather connected with transient effects (see Section 4.8).

5.2.4. Slag thermal conductivity profiles

The slag thermal conductivity profiles for the bioliq EFG experiment V82 and the segment 3 are shown in Fig. 18. The profile based on the derived data spans from 0.9 W/(m K) to 1.9 W/(m K); it is thus difficult to approximate the slag thermal conductivity using a constant value without detailed heat transfer analysis. Future studies should therefore avoid assumptions for the slag thermal conductivity and should rely on measured data (see Section 5.2.2).

5.2.5. Slag velocity profiles

The slag velocity profiles for the bioliq EFG experiment V82 and the segment 3 were derived using the common gravity-driven steady-state film flow model and either the derived thermal conductivity data or constant thermal conductivity values (0.7 W/(m K), 1.5 W/(m K), 1.9 W/(m K)). The profiles are depicted in Fig. 19 and show that the slag layer does not exhibit two distinct layers, i. e. a solid and a liquid layer. This is due to the glassy nature of slag V82 (see Section 4.5). Solid and liquid slag layers should therefore not be assumed for all slags, in contrast to typical slag flow modelling approaches, which are based on a critical slag viscosity or a temperature of critical slag viscosity. Measured slag viscosity and thermal conductivity data should be used to scrutinise the approach.

[2] The WGS temperature at position B $T_{WGS,B}$ is close to the gas temperature at position B if (i) a partial WGS equilibrium is expected for position B, (ii) the gas temperature is below the freezing temperature and (iii) the WGS temperature is calculated using the gas composition at position B [6]. The WGS temperature is not affected by the energy balances of the reactor chamber and thus reflects peripheral heat losses [6].

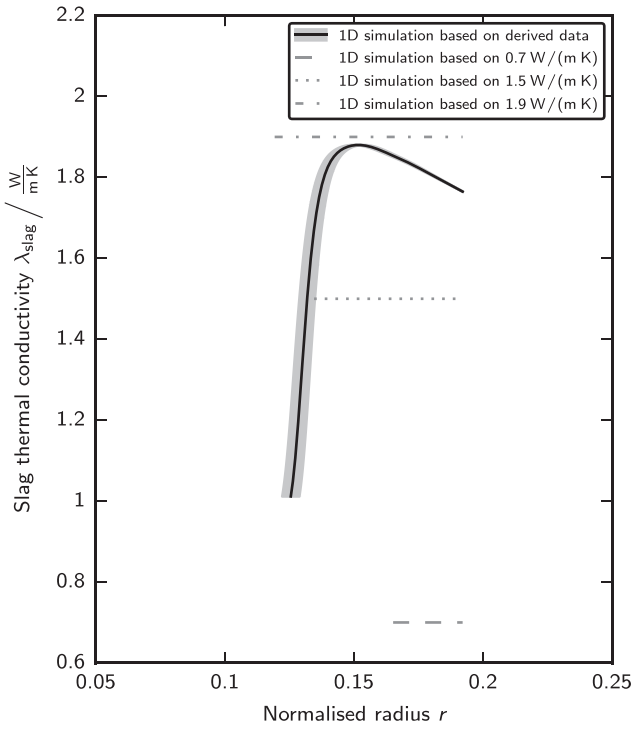

Fig. 18. Slag thermal conductivity profiles for the bioliq EFG experiment V82 and segment 3.

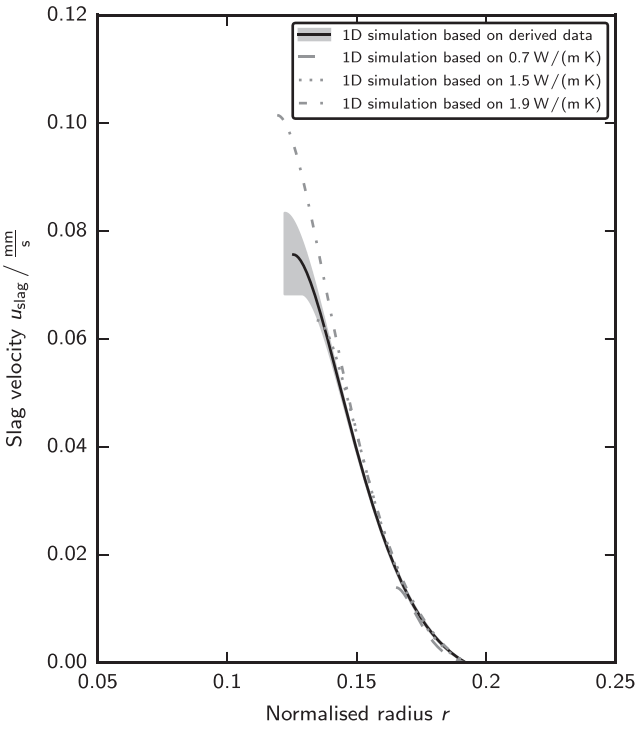

Fig. 19. Slag velocity profiles for the bioliq EFG experiment V82 and segment 3.

5.2.6. Wall and slag temperature profiles

The wall and slag temperature profiles were studied using either the derived thermal conductivity data or constant thermal conductivity values (0.7 W/(m K), 1.5 W/(m K), 1.9 W/(m K)). The predicted wall and slag temperature profiles are shown for the bioliq EFG experiments V82, V83 and V84 and the segments 2 and 3 in Figs. 20–22. In addition,

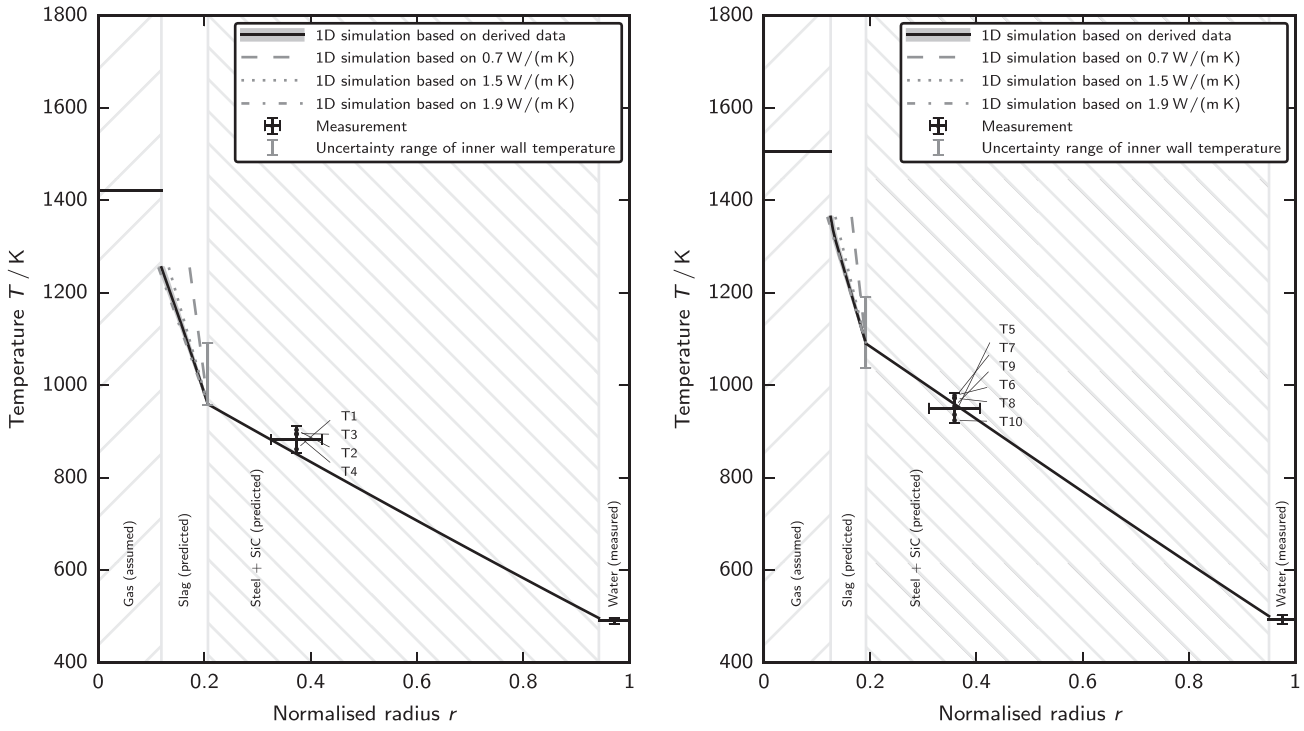

Fig. 20. Wall and slag temperature profiles for the bioliq EFG experiment V82 and segment 2 (left) and segment 3 (right).

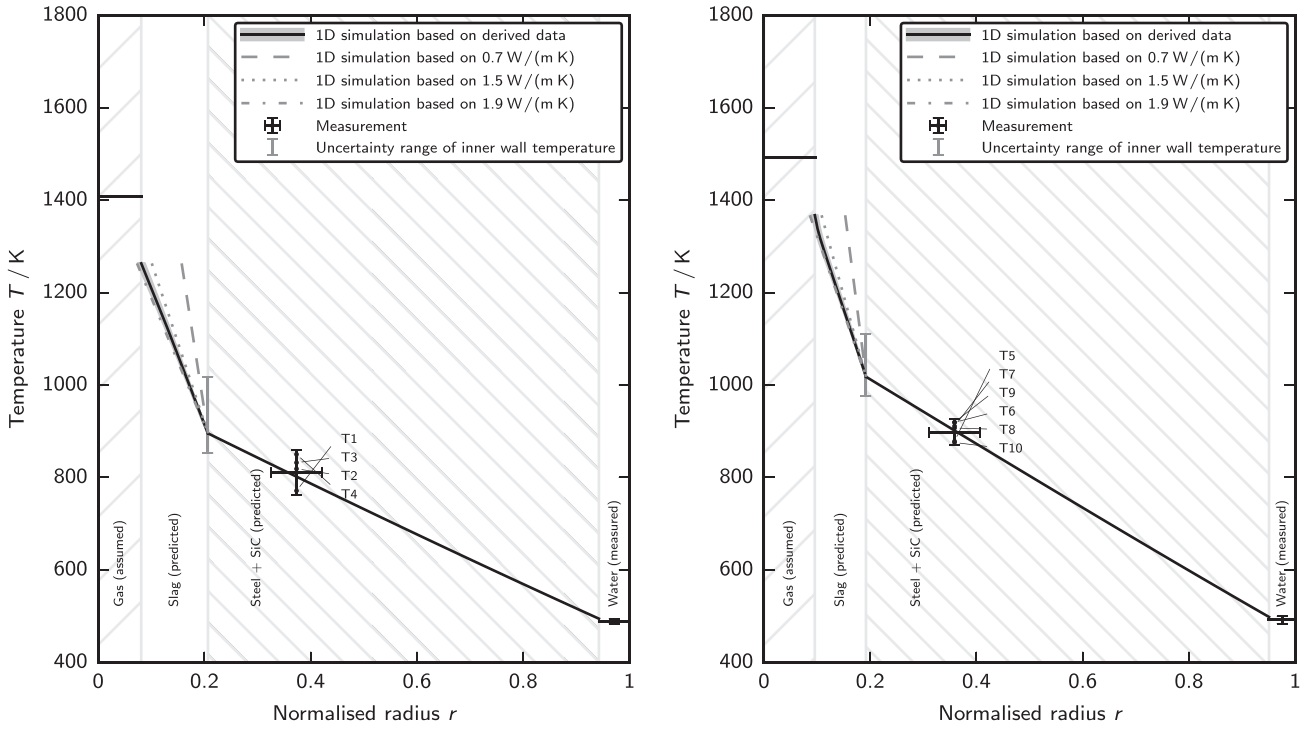

Fig. 21. Wall and slag temperature profiles for the bioliq EFG experiment V83 and segment 2 (left) and segment 3 (right).

horizontal lines represent the water and gas boundary temperatures, and grey areas highlight the uncertainty ranges of the slag temperature profiles that are obtained using the derived data. The uncertainty ranges reflect the uncertainties in the measured slag thermal conductivity of ±5% (see Section 3.7). Furthermore, the temperatures measured using thermocouples at positions T1, …, T10 (see Fig. 2 and [6]) are shown in Figs. 20–22. The uncertainties in these temperatures were calculated using the measured data and assuming ±3 mm as uncertainty of the thermocouple positions[3]. Finally, as the comparison of measured and predicted wall temperatures is restricted through the assumption

[3] The exact positions of the thermocouples are not known in contrast to previous statements [51].

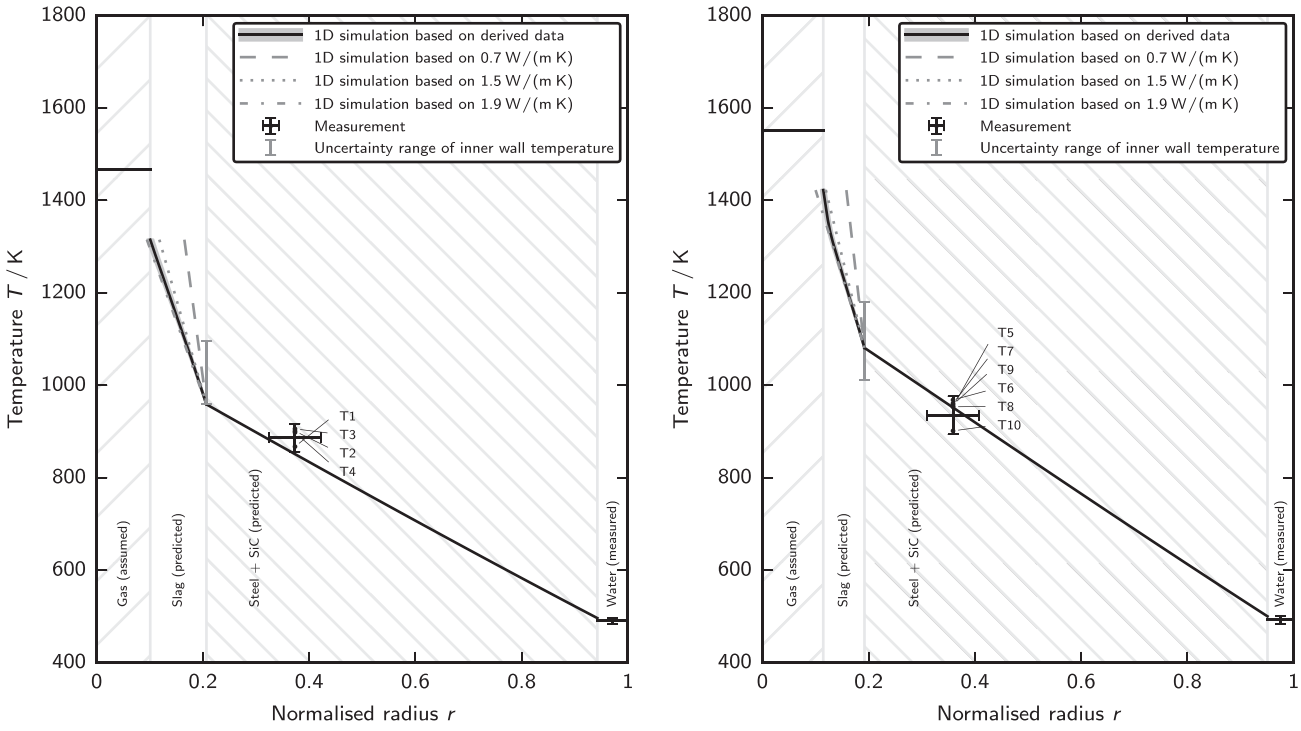

Fig. 22. Wall and slag temperature profiles for the bioliq EFG experiment V84 and segment 2 (left) and segment 3 (right).

of a homogeneous wall layer, uncertainty bars are shown for the inner wall temperatures in Figs. 20–22. The uncertainty bars were determined based on extrapolation of the measured temperatures. The extrapolation was implemented expecting that only SiC is placed between the slag and the thermocouple tip, i. e. using the SiC thermal conductivity instead of the effective wall thermal conductivity. The findings based on the measured and predicted temperatures are summarised below:

1. The predicted wall temperature profiles are almost linear due to the simplified thermal conductivity approach and the small temperature dependence of the wall thermal conductivity.
2. The predicted slag temperature profiles based on the derived data are clearly non-linear, in contrast to usual assumptions of linear slag temperature profiles for slag flow simulations.
3. The predicted wall temperatures were appropriately adjusted to the measured temperatures using the thermal resistance approach based on series, Maxwell and parallel models.
4. The predicted inner wall temperatures are afflicted with high uncertainties due to the uncertainties related to the thermocouple positions and the composition of the cooling screen.
5. The slag properties and the wall structures determine the temperature distribution between cooling water and inner reactor chamber.

5.3. Possible applications

This section discusses the use of the derived slag property data for model development and validation as well as the use of the segmental slag layer model for process monitoring and balancing.

5.3.1. Model validation

The analyses, measurements and simulations were conducted assuming that the derived data can be used for describing the slag properties in numerical simulations of the bioliq EFG experiments V82, V83, V84 and V85. However, some comments and comparisons are necessary to justify this approach:

1. The analyses and measurements of the material properties were conducted after removal of chemically dissolved gases. The quantitative influences of these gases are unknown at this stage (see Section 5.1.1). Therefore, the slag property models do not account for this effect.
2. The density measurements at ambient temperatures and the morphology analyses showed only tiny amounts of physical gas enclosures (see Section 4.3). Therefore, the slag property models do not need to reflect them.
3. The density analyses at ambient temperatures showed fairly similar densities for the discharged and deposited slags (see Section 4.3). Therefore, the properties of the deposited slag V82 can be described using the properties of the discharged slag V82.
4. The chemical analyses and the melting analyses indicated similar material properties for the samples of discharged slags V82, V83, V84 and V85 (see Sections 4.1 and 4.2).

In conclusion, the thermo-physical property data derived for slag V82 may be used to describe the slag properties in numerical simulations of the bioliq EFG experiments V82, V83, V84 and V85. Furthermore, chemical compositions, melting temperatures and slag thicknesses as well as experimental, balancing and equilibrium data [6] are available as input and validation data. The preceding study and the present study thus provided several consistent and unique data sets for the development and validation of high-pressure entrained flow gasification models with surrogate suspension fuels. This in particular stresses again that glass beads were used instead of technical ashes. This was done in order to minimise catalytic effects and material variability over long operating times (more than 130 h in total), while accepting different chemical and physical properties compared to biogenic or anthropogenic ashes. For example, ashes from straw derivatives have consisted mainly of 55–61% SiO_2, 20–24% K_2O and 10–12% CaO and have thus exhibited high contents of K_2O, which was partially released as volatile matter in high-pressure entrained flow gasification experiments [7]. Moreover, the discharged biomass slags showed lower densities and surface tensions [7] compared to slag V82. Therefore, the glass slag property data compiled in

this study can usually not be adapted to slags from other feedstocks, e. g. biomass. However, in the absence of complete, consistent and superior slag property data, the data compiled could still be used for design and scale-up of high-pressure entrained flow gasification processes with biogenic or anthropogenic pyrolysis oils that typically exhibit low ash contents.

5.3.2. Process monitoring and balancing

The operating and process conditions in gasification plants are typically monitored using various quantities. For the bioliq EFG experiment V83, the measured dry gas-species concentrations at position C (see Fig. 1 and [6]) and the pseudo-steady-state water-gas-shift temperatures are shown in Fig. 23. These curves show quasi-stationary

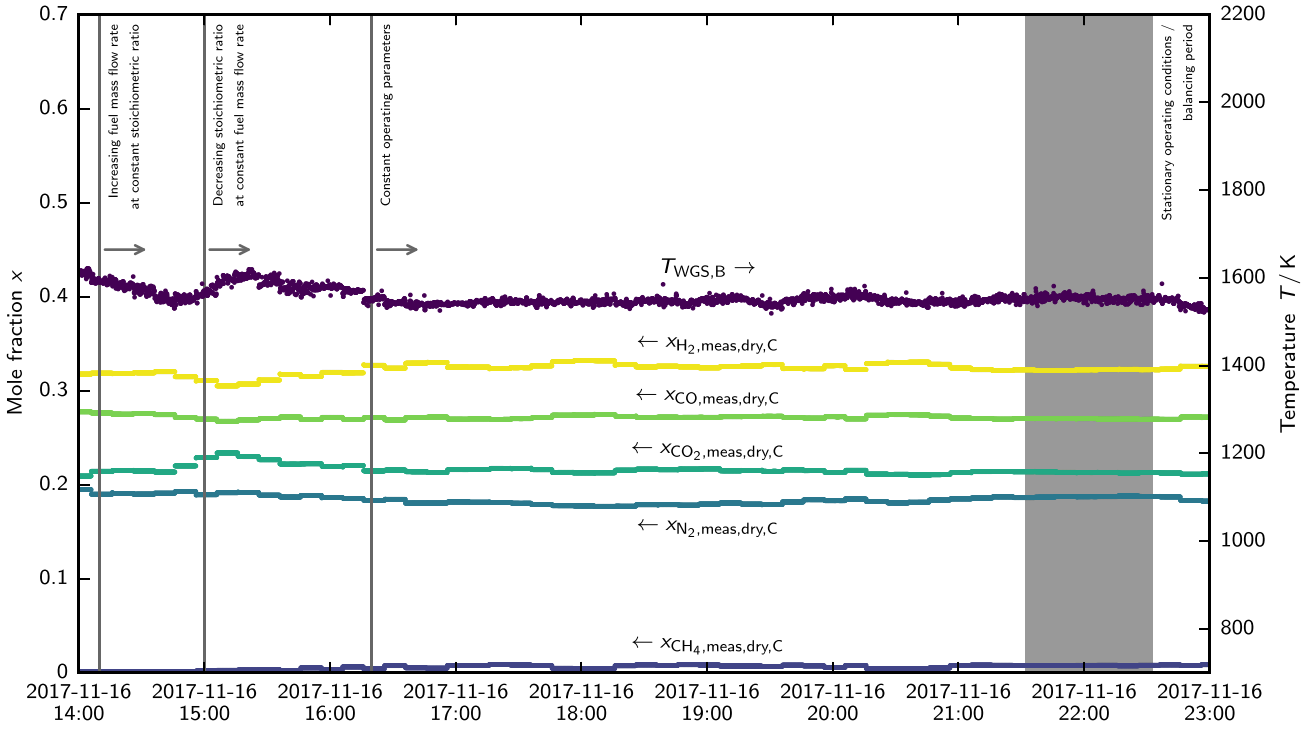

Fig. 23. Time histories of gas-species concentrations measured at position C in mole fractions $\boldsymbol{x}_{\mathrm{meas,dry,C}}$ and water-gas-shift temperatures at position B $T_{\mathrm{WGS,B}}$: comparison for the bioliq EFG experiment V83.

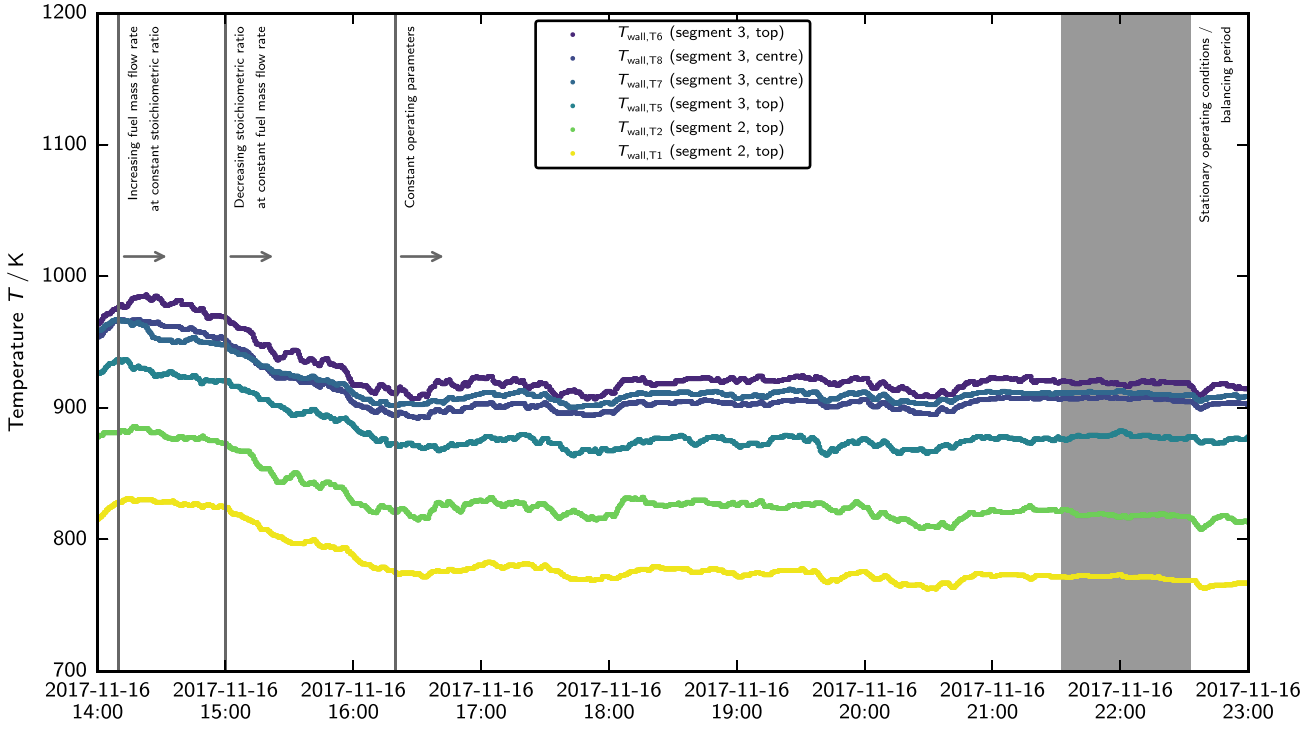

Fig. 24. Time histories of refractory temperatures measured at positions T1, T2, T5, T6, T7 and T8: comparison for the bioliq EFG experiment V83.

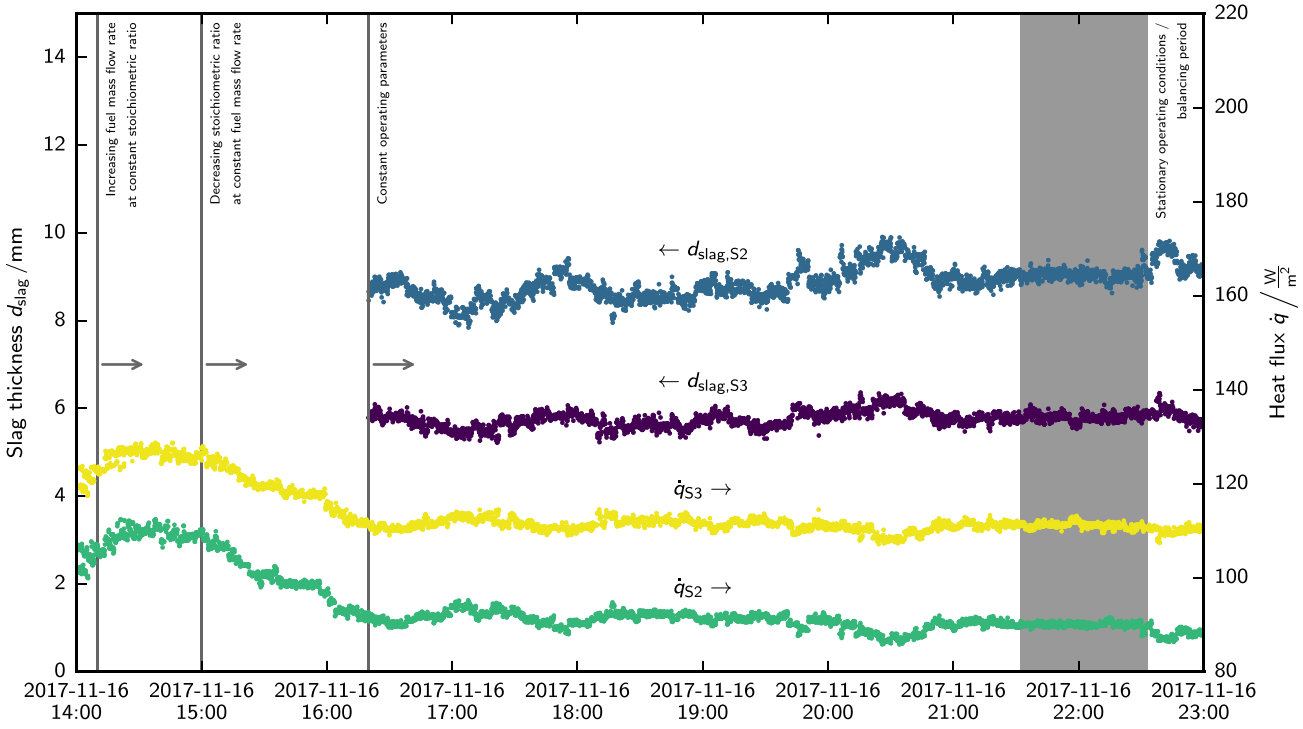

Fig. 25. Time histories of slag thicknesses predicted for segment 2 $d_{slag,S2}$ and for segment 3 $d_{slag,S3}$ and heat fluxes balanced for segment 2 $\dot{q}_{S2}$ and for segment 3 $\dot{q}_{S3}$: comparison for the bioliq EFG experiment V83.

gas-phase conditions for extended periods with constant operating parameters. In addition, the measured refractory temperatures (see Fig. 2 and [6]) as well as the heat fluxes derived for segments 2 and 3 (see Fig. 2 and [6]) are shown in Figs. 24 and 25. These curves, in turn, indicate approximately constant heat extractions but also strongly fluctuating refractory temperatures in the period with constant operating parameters. Therefore, monitoring of measured data as well as data derived from mass and energy balances does not always support the evaluation of the slag flow behaviour during plant operation and the identification of appropriate periods of time with approximately stationary conditions (balancing periods). Moreover, the slag flow and the slag thickness can currently not be monitored online using experimental methods. Therefore, simplified modelling approaches may be used instead. In this study, a slag layer model was implemented following Eqs. (1)–(5). This model assumes the WGS temperature as gas temperature, neglects energy accumulation for both slag and refractory and was tested using the process data of the bioliq EFG experiment V83. For the period with constant operating parameters, the predicted slag thicknesses are shown in Fig. 25. Firstly, the predictions for segment 3 and the balancing period are similar to the results shown in Fig. 16, while those for segment 2 are higher because the assumed gas temperatures (i. e. the water-gas-shift temperatures) are 100–200 K higher than the temperatures prevailing in the boundary of segment 2. Secondly, the predictions show less fluctuations in the selected balancing period than in the periods before. This confirms the trends of the water-gas-shift temperature and the heat fluxes and shows the best possible selection of the balancing period. Moreover, it demonstrates that simplified modelling approaches are useful tools to monitor the slag behaviour during plant operation and to determine appropriate balancing periods.

6. Conclusions

Surrogate slag property data were derived for the development and validation of slag flow models, required for numerical simulations of (technical) slagging entrained flow gasifiers. The data were generated in the course of four bioliq EFG experiments with mixtures of ethylene glycol and glass beads as well as pyrolysis oil and glass beads at thermal inputs of up to 5 MW and operating pressures of 40 bar. Ethylene glycol and glass beads were used in order to derive experimental data under well-defined conditions and enable numerical modelling for well-defined feedstocks. The outcomes of this study are summarised below:

1. Measured data of chemical and physical slag properties including composition, melting behaviour, density, surface tension, dynamic viscosity, thermal conductivity and specific heat capacity
2. Data of slag thickness measured at four refractory positions after completing three pilot-scale experiments (i. e. under ambient conditions after reactor shut-down)
3. One-dimensional slag layer model based on appropriately simplified geometry and derived process and slag property data
4. Analysis of slag thickness based on the measured and predicted data for stationary and quasi-stationary conditions
5. Analysis of slag temperature and velocity profiles based on derived or constant slag thermal conductivity data

The slag property data are complemented by experimental, balancing and equilibrium data, which are given in the preceding study [6]. To the best knowledge of the authors, these are the only complete and consistent data sets for pilot-scale entrained flow gasifiers. Even though the data sets were not derived for technical feedstocks but for surrogate suspension fuels, future studies may use them to develop and validate high-pressure entrained flow gasification models. In addition, detailed slag flow simulations of the bioliq EFG experiments may be conducted using the volume-of-fluid method (see [8,26,30]) or the smoothed-particle-hydrodynamics method (see [43,44]) in order to analyse transient slag flow effects during stationary conditions. Detailed (three-dimensional) simulations may also focus on the heat transfer between cooling medium and inner reactor chamber, accounting for the complex refractory structures, in order to develop simplified approaches

following previous works [34,115]. Furthermore, experimental studies may use the outcomes of this study as motivation to develop online methods for measuring slag thicknesses under process conditions and to analyse material properties of technical slags using novel pressurised setups.

CRediT authorship contribution statement

Maximilian Dammann: Writing – review & editing, Writing – original draft, Visualisation, Validation, Supervision, Software, Methodology, Investigation, Formal analysis, Data curation, Conceptualisation. **Stella Clara Walker:** Writing – review & editing, Writing – original draft, Visualisation, Validation, Methodology, Investigation, Conceptualisation. **Michael Müller:** Writing – review & editing, Validation, Methodology, Investigation, Formal analysis. **Ulrike Santo:** Writing – review & editing, Visualisation, Validation, Methodology, Investigation, Formal analysis. **Hannah Knoch:** Writing – review & editing, Methodology, Investigation. **Mark Eberhard:** Methodology, Investigation. **Marco Mancini:** Supervision. **Thomas Kolb:** Writing – review & editing, Supervision, Project administration, Funding acquisition.

Declaration of competing interest

The authors declare that they have no known competing financial interests or personal relationships that could have appeared to influence the work reported in this paper.

Acknowledgements

The authors thank (i) the German Federal Ministry for Food and Agriculture (BMEL) as represented by the Fachagentur für Nachwachsende Rohstoffe (FNR), the Helmholtz Association of German Research Centres (HGF) and the Baden Württemberg State Ministry of Economic Affairs, Labour and Housing for financing the bioliq plant, (ii) Air Liquide Engineering & Construction for financial participation and for building the bioliq EFG plant, (iii) the Helmholtz Association of German Research Centres (HGF) for funding the programmes Energy Efficiency, Materials and Resources (EMR), Renewable Energies (EE) and Materials and Technologies for the Energy Transition (MTET) and for funding the Helmholtz Virtual Institute for Gasification Technology (HVIGasTech, VH-VI-429), (iv) the operating team of the bioliq plant under the leadership of Bernd Zimmerlin and Bernd Michelfelder (Karlsruhe Institute of Technology, Institute for Technical Chemistry, Energy Laboratories) for conducting the bioliq EFG campaigns, (v) Herbert Fischer (formerly Karlsruhe Institute of Technology, Institute for Technical Chemistry, Pyrolysis/Gas Treatment), Britta Bergfeldt and Angela Ullrich (Karlsruhe Institute of Technology, Institute for Technical Chemistry, Technical Mineralogy), Stefanie Kaufmann (formerly Karlsruhe Institute of Technology, Institute for Technical Chemistry, Technical Mineralogy), Volker Zibat (formerly Karlsruhe Institute of Technology, Light Technology Institute), and Frank Hemberger and his team (ZAE Bayern, Energy Efficiency, Thermal Analysis) for the experimental support, (vi) David Böning for curating process and balancing data, and (vii) Guixuan Wu and Konrad Mielke (formerly Forschungszentrum Jülich, Institute of Energy and Climate Research, Microstructure and Properties of Materials) for their preceding works.

Supplementary material

Supplementary material to this article can be found online at 10.1016/j.fuel.2026.139480.

Data availability

Data will be made available on request.

References

[1] DIN Deutsches Institut für Normung. DIN 51730:1998-04. Prüfung fester Brennstoffe. Bestimmung des Asche-Schmelzverhaltens; Apr 1998.
[2] DIN Deutsches Institut für Normung. DIN 51730:2007-09. Prüfung fester Brennstoffe. Bestimmung des Asche-Schmelzverhaltens; Sep 2007.
[3] Dahmen N, Abeln J, Eberhard M, Kolb T, Leibold H, Sauer J, Stapf D, Zimmerlin B. The bioliq process for producing synthetic transportation fuels. Wires Energy Environ 2016;6(3). https://doi.org/10.1002/wene.236.
[4] Eberhard M, Santo U, Michelfelder B, Günther A, Weigand P, Matthes J, Waibel P, Hagenmeyer V, Kolb T. The bioliq® Entrained Flow Gasifier: A model for the German Energiewende. ChemBioEng Rev 2020;7(4):106–18. https://doi.org/10.1002/cben.202000006.
[5] Hennig M, Dreising TM, Reeves A, Oehlcke T, Tavakkol S, Volk R, Schultmann F, Stapf D. Entrained-flow gasification for the utilization of pyrolysis oil from mixed plastic waste. ACS Sustain Chem Eng 2025;13(48):20638–48. https://doi.org/10.1021/acssuschemeng.5c03932.
[6] Dammann M, Santo U, Böning D, Knoch H, Eberhard M, Kolb T. Entrained flow gasification: Pilot-scale experimental, balancing and equilibrium data for model validation. Fuel, Part A 2025;382:132809. https://doi.org/10.1016/j.fuel.2024.132809.
[7] Seebold S, Eberhard M, Wu G, Yazhenskikh E, Sergeev D, Kolb T, Müller M. Thermophysical and chemical properties of bioliq slags. Fuel 2017;197:596–604. https://doi.org/10.1016/j.fuel.2017.02.027.
[8] Chen L, Yong SZ, Ghoniem AF. Modeling the slag behavior in three dimensional CFD simulation of a vertically-oriented oxy-coal combustor. Fuel Process Technol 2013;112:106–17. https://doi.org/10.1016/j.fuproc.2013.02.010.
[9] Ni J, Yu G, Guo Q, Zhou Z, Wang F. Submodel for predicting slag deposition formation in slagging gasification systems. Energy Fuels 2011;25(3):1004–9. https://doi.org/10.1021/ef101696a.
[10] Yong SZ, Gazzino M, Ghoniem A. Modeling the slag layer in solid fuel gasification and combustion: Formulation and sensitivity analysis. Fuel 2012;92(1):162–70. https://doi.org/10.1016/j.fuel.2011.06.062.
[11] Yong SZ, Ghoniem A. Modeling the slag layer in solid fuel gasification and combustion: Two-way coupling with CFD. Fuel 2012;97:457–66. https://doi.org/10.1016/j.fuel.2012.02.063.
[12] Lin K, Shen Z, Liang Q, Xu J, Guo X, Liu H. The study of slag discharge behavior of entrained-flow gasifier based on the viscosity-temperature characteristics of different types of coals. Fuel 2021;292:120314. https://doi.org/10.1016/j.fuel.2021.120314.
[13] Lin K, Shen Z, Liang Q, Dai Z, Xu J, Guo X, Liu H. The effect of coal viscosity-temperature characteristics on the dynamic response of slag discharge behavior in Shell gasifier. Fuel 2022;307:121796. https://doi.org/10.1016/j.fuel.2021.121796.
[14] Mielke K, Wu G, Eberhard M, Kolb T, Müller M. Optimization of slag mobility of biomass fuels in a pilot-scale entrained-flow gasifier. Chem Eng Technol 2021;44(7):1302–10. https://doi.org/10.1002/ceat.202000531.
[15] Zhang B, Shen Z, Liang Q, Xu J, Liu H. Modeling the slag flow and heat transfer with the effect of fluid-solid slag layer interface viscosity in an entrained flow gasifier. Appl Therm Eng 2017;122:785–93. https://doi.org/10.1016/j.applthermaleng.2017.04.095.
[16] Reid WT, Cohen P. Factors affecting the thickness of coal-ash slag on furnace-wall tubes. Trans ASME 1944;66(8):685–90. https://doi.org/10.1115/1.4018149.
[17] Reid WT, Cohen P. The flow characteristics of coal-ash slags in the solidification range. In: Proceedings of the Annual Meeting of the ASME, 29 November-3 December 1943. New York, NY, USA; 1944. p. 83–97.
[18] Cohen P, Reid WT. The flow of coal-ash slag on furnace walls. Tech. Rep. 663; Washington D.C., USA: United States Bureau of Mines, United States Department of the Interior; Nov 1944. https://books.google.de/books?id=8T8r3LwsMa4C.
[19] Schoen P. Dynamic modeling and control of integrated coal gasification combined cycle units [Ph.D. thesis]. Delft, The Netherlands: Delft University of Technology; Sep 1993. http://resolver.tudelft.nl/uuid:59ae88a4-b5cf-4c71-83e7-c8df8873b6b1.
[20] Beath AC. Mathematical modelling of entrained flow coal gasification [Ph.D. thesis]. Newcastle, NSW, Australia: Department of Chemical Engineering, University of Newcastle; Mar 1996. http://hdl.handle.net/1959.13/24844.
[21] Seggiani M. Modelling and simulation of time varying slag flow in a Prenflo entrained-flow gasifier. Fuel 1998;77(14):1611–21. https://doi.org/10.1016/s0016-2361(98)00075-1.
[22] Benyon PJ, Inumaru J, Otaka M, Hara S, Watanabe H. Computational modelling of entrained flow slagging gasifiers. In: Proceedings of the 10th Japan–Australia Joint Technical Meeting on Coal, December 2000; Fukuoka, Japan; 2000.
[23] Benyon PJ. Computatonal modelling of entrained flow slagging gasifiers [Ph.D. thesis]. Sydney, NSW, Australia: School of Aerospace, Mechanical & Mechatronic Engineering, University of New South Wales; Mar 2002. http://hdl.handle.net/2123/1276.
[24] Bockelie MJ, Denison MK, Chen Z, Linjewile T, Senior CL, Sarofim AF, Holt N. CFD modeling for entrained flow gasifiers. In: Proceedings of the Gasification Technologies Conference, 27–30 October 2002; San Francisco, CA, USA; Mar 2002. https://collections.lib.utah.edu/ark:/87278/s63b8z7n.
[25] Otaka M, Watanabe H, Hara S. Numerical simulation of molten-slag flow in coal gasifier. In: Proceedings of the ASME 2005 Power Conference, 5–7 April 2005; Chicago, IL, USA; 2005. no. PWR2005-50370, p. 1471–6. https://doi.org/10.1115/pwr2005-50370.

[26] Liu S, Hao Y. Numerical study on slag flow in an entrained-flow gasifier. In: Proceedings of the ASME 2007 International Mechanical Engineering Congress and Exposition. Volume 6: Energy Systems: Analysis, Thermodynamics and Sustainability, 11–15 November 2007; Seattle, WA, USA: ASME Digital Collection; 2007. no. IMECE2007-43310, p. 793–800. https://doi.org/10.1115/imece2007-43310.

[27] Wang XH, Zhao DQ, He LB, Jiang LQ, He Q, Chen Y. Modeling of a coal-fired slagging combustor: Development of a slag submodel. Combust Flame 2007;149(3):249–60. https://doi.org/10.1016/j.combustflame.2007.02.001.

[28] Kittel J, Hannemann F, Mehlhose F, Heil S, Meyer B. Dynamic modelling of the heat transfer into the cooling screen of the SFGT-Gasifier. In: Proceedings of the 7th International Modelica Conference, 20–22 September 2009; Como, Italy: Linköping University Electronic Press; 2009. p. 326–34. https://doi.org/10.3384/ecp09430011.

[29] Li B, Brink A, Hupa M. Simplified model for determining local heat flux boundary conditions for slagging wall. Energy Fuels 2009;23(7):3418–22. https://doi.org/10.1021/ef800957k.

[30] Ni J, Zhou Z, Yu G, Liang Q, Wang F. Molten slag flow and phase transformation behaviors in a slagging entrained-flow coal gasifier. Ind Eng Chem Res 2010;49(23):12302–10. https://doi.org/10.1021/ie1013844.

[31] Yong SZ. Multiphase models of slag layer built-up in solid fuel gasification and combustion [Master's thesis]. Cambridge, MA, USA: Department of Mechanical Engineering, Massachusetts Institute of Technology; Jun 2010. http://hdl.handle.net/1721.1/61928.

[32] Sun B, Liu Y, Chen X, Zhou Q, Su M. Dynamic modeling and simulation of Shell gasifier in IGCC. Fuel Process Technol 2011;92(8):1418–25. https://doi.org/10.1016/j.fuproc.2011.02.017.

[33] Chung J, Chi J, Lee J, Seo S, Kim K, Park H. Analysis of slag behavior near the slag tap in an entrained flow coal gasifier. Transactions of the Korean Hydrogen and New Energy Society 2011;22(6):913–24. https://doi.org/10.7316/khnes.2011.22.6.913.

[34] Liang Q, Guo X, Dai Z, Liu H, Gong X. An investigation on the heat transfer behavior and slag deposition of membrane wall in pilot-scale entrained-flow gasifier. Fuel 2012;102:491–8. https://doi.org/10.1016/j.fuel.2012.06.092.

[35] Wang J, Liu H, Liang Q, Xu J. Experimental and numerical study on slag deposition and growth at the slag tap hole region of shell gasifier. Fuel Process Technol 2013;106:704–11. https://doi.org/10.1016/j.fuproc.2012.10.005.

[36] Bi D, Guan Q, Xuan W, Zhang J. Combined slag flow model for entrained flow gasification. Fuel 2015;150:565–72. https://doi.org/10.1016/j.fuel.2015.02.028.

[37] Pednekar P, Bhattacharyya D, Kasule JS, Turton R, Rengaswamy R. Dynamic model of a slagging entrained-flow gasifier including models of slag transport, deposition, and slag layer. Ind Eng Chem Res 2016;55(1):279–92. https://doi.org/10.1021/acs.iecr.5b03317.

[38] Safronov D, Förster T, Richter A, Nikrityuk P, Bronsch A, Schwitalla D, Guhl S, Meyer B. Subgrid model for slag behaviour at entrained flow gasifier walls. In: Proceedings of the 27th Deutscher Flammentag: Verbrennung und Feuerung, 16–17 September 2015; Clausthal-Zellerfeld, Germany: Deutsche Vereinigung für Verbrennungsforschung and The Combustion Institute Deutsche Sektion; Düsseldorf, Germany: VDI-Verlag; 2015. vol. 2267 of VDI-Berichte, p. 563–8.

[39] Ye I, Ryu C. Numerical modeling of slag flow and heat transfer on the wall of an entrained coal gasifier. Fuel 2015;150:64–74. https://doi.org/10.1016/j.fuel.2015.01.111.

[40] Ye I, Oh J, Ryu C. Effects of design/operating parameters and physical properties on slag thickness and heat transfer during coal gasification. Energies 2015;8(5):3370–85. https://doi.org/10.3390/en8053370.

[41] Ye I, Ryu C, Koo JH. Influence of critical viscosity and its temperature on the slag behavior on the wall of an entrained coal gasifier. Appl Therm Eng 2015;87:175–84. https://doi.org/10.1016/j.applthermaleng.2015.05.027.

[42] Bhuiyan AA, Naser J. Modelling of slag deposition and flow characteristics of coal combustion under oxy-firing condition in a 550 MW tangentially fired furnace. Appl Therm Eng 2016;106:221–35. https://doi.org/10.1016/j.applthermaleng.2016.05.180.

[43] Kurowski M-P, Spliethoff H. Deposition and slag flow modeling with SPH for a generic gasifier with different coal ashes using fusibility data. Fuel 2016;172:218–27. https://doi.org/10.1016/j.fuel.2016.01.020.

[44] Kurowski M-P, Spliethoff H. Deposition and slagging in an entrained-flow gasifier with focus on heat transfer, reactor design and flow dynamics with SPH. Fuel Process Technol 2016;152:147–55. https://doi.org/10.1016/j.fuproc.2016.06.029.

[45] Xu J, Liang Q, Dai Z, Liu H. Comprehensive model with time limited wall reaction for entrained flow gasifier. Fuel 2016;184:118–27. https://doi.org/10.1016/j.fuel.2016.06.122.

[46] Melchiori T, Boulet M, Lavoie J-M. Modeling of ash deposition on the wall of a high temperature slagging gasifier. Fuel 2017;197:100–10. https://doi.org/10.1016/j.fuel.2017.02.017.

[47] Kim M, Ye I, Ryu C. Numerical analysis on transient behaviors of slag layer in an entrained-flow coal gasifier. Fuel 2017;196:532–42. https://doi.org/10.1016/j.fuel.2017.02.002.

[48] Safronov D, Förster T, Schwitalla D, Nikrityuk P, Guhl S, Richter A, Meyer B. Numerical study on entrained-flow gasification performance using combined slag model and experimental characterization of slag properties. Fuel Process Technol 2017;161:62–75. https://doi.org/10.1016/j.fuproc.2017.03.007.

[49] Xu J, Dai Z, Liu H, Guo L, Sun F. Modeling of multiphase reaction and slag flow in single-burner coal water slurry gasifier. Chem Eng Sci 2017;162:41–52. https://doi.org/10.1016/j.ces.2016.12.029.

[50] Zhang B, Shen Z, Han D, Liang Q, Xu J, Liu H. Effects of the bubbles in slag on slag flow and heat transfer in the membrane wall entrained-flow gasifier. Appl Therm Eng 2017;112:1178–86. https://doi.org/10.1016/j.applthermaleng.2016.10.141.

[51] Cavagnol SM, Covella K, Müller-Hagedorn M. Determination of slag deposition rate on cooling screen reactor walls by utilisation of slag thickness measurements. Fuel 2018;228:369–78. https://doi.org/10.1016/j.fuel.2018.04.089.

[52] Kim M, Ye I, Ryu C. Effect of slag viscosity model on transient simulations of wall slag flow in an entrained coal gasifier. Korean J Chem Eng 2018;35(5):1065–72. https://doi.org/10.1007/s11814-018-0008-x.

[53] Zhang B, Shen Z, Liang Q, Xu J, Liu H. Modeling study of residence time of molten slag on the wall in an entrained flow gasifier. Fuel 2018;212:437–47. https://doi.org/10.1016/j.fuel.2017.10.073.

[54] Zhang B, Shen Z, Liang Q, Xu J, Liu H. Numerical study of dynamic response analysis of slag behaviors in an entrained flow gasifier. Fuel 2018;234:1071–80. https://doi.org/10.1016/j.fuel.2018.07.152.

[55] Zhang B, Shen Z, Liang Q, Xu J, Liu H. Modeling the slag flow and heat transfer on the bottom cone of a membrane wall entrained-flow gasifier. Fuel 2018;226:1–9. https://doi.org/10.1016/j.fuel.2018.03.194.

[56] Ge J, Wang Z, Wan K, He Y, Zhou Z, Huang Z. Slagging behavior modeling in coal gasifiers using two-way coupled slag model with CFD. Fuel 2020;281:118736. https://doi.org/10.1016/j.fuel.2020.118736.

[57] Zhang B, Jin J, Liu H. Modeling study of the slag behaviors and SiC refractory wall corrosion on the top cone of a membrane wall entrained-flow gasifier. Energy Fuels 2020;34(10):12440–8. https://doi.org/10.1021/acs.energyfuels.0c02477.

[58] Lin K, Shen Z, Liang Q, Xu J, Liu H. Modelling of slag flow and prediction of corrosion state of refractory bricks in an entrained-flow gasifier. Fuel 2020;275:117979. https://doi.org/10.1016/j.fuel.2020.117979.

[59] Lin K, Shen Z, Liang Q, Xu J, Liu H. Modelling study of characteristics of heat transfer and structural optimization of refractory layer in an entrained-flow gasifier. Appl Therm Eng 2020;168:114830. https://doi.org/10.1016/j.applthermaleng.2019.114830.

[60] Dammann M, Mancini M, Weber R, Kolb T. Entrained flow gasification: Mathematical modelling based on RANS for design and scale-up. In: Proceedings of the 30th Deutscher Flammentag: für nachhaltige Verbrennung, 28–29 September 2021; Hannover-Garbsen, Germany: Deutsche Vereinigung für Verbrennungsforschung and The Combustion Institute Deutsche Sektion, Hannover-Garbsen; 2021. https://doi.org/10.5445/IR/1000140359.

[61] Allibert M. Slag atlas. 2nd ed. Düsseldorf, Germany: Verlag Stahleisen; 1995.

[62] Anderson DW, Viskanta R, Incropera FP. Effective thermal conductivity of coal ash deposits at moderate to high temperatures. J Eng Gas Turbines Power 1987;109(2):215–21. https://doi.org/10.1115/1.3240027.

[63] Bottinga Y, Weill DF. Densities of liquid silicate systems calculated from partial molar volumes of oxide components. Am J Sci 1970;269(2):169–82. https://doi.org/10.2475/ajs.269.2.169.

[64] Hurst HJ, Novak F, Patterson JH. Viscosity models for fluxed Australian bituminous coal ashes. In: Proceedings of the 5th International Conference on Molten Slags, Fluxes, and Salts, 5–8 January 1997; Sydney, NSW, Australia; 1997. p. 873–6. https://pyro.co.za/MoltenSlags1997/873-Hurst.pdf.

[65] Kalmanovitch DP, Frank M. An effect model of viscosity for ash deposition phenomena. In: Bryers RW, Vorres KS, editors. Proceedings of the Engineering Foundation Conference on Mineral Matter and Ash Deposition from Coal, 22–26 February 1988; Santa Barbara, CA, USA; 1988. p. 89–101.

[66] Lange RA, Carmichael ISE. Densities of Na_2O–K_2O–CaO–MgO–FeO–Fe_2O_3–Al_2O_3–TiO_2–SiO_2 liquids: New measurements and derived partial molar properties. Geochim Cosmochim Acta 1987;51(11):2931–46. https://doi.org/10.1016/0016-7037(87)90368-1.

[67] Mills KC, Rhine JM. The measurement and estimation of the physical properties of slags formed during coal gasification. 1. Properties relevant to fluid flow. Fuel 1989;68(2):193–200. https://doi.org/10.1016/0016-2361(89)90322-0.

[68] Mills KC, Rhine JM. The measurement and estimation of the physical properties of slags formed during coal gasification. 2. Properties relevant to heat transfer. Fuel 1989;68(7):904–10. https://doi.org/10.1016/0016-2361(89)90128-2.

[69] Sage WL, McIlroy JB. Relationship of coal-ash viscosity to chemical composition. J Eng Power 1960;82(2):145–53. https://doi.org/10.1115/1.3672737.

[70] Streeter RC, Diehl EK, Schobert HH. Measurement and prediction of low-rank coal slag viscosity. In: Preprints of papers presented at the Notital Meeting of the American Chemical Society, Division of Fuel Chemistry; 1983. vol. 28, no. 4, p. 174–95.

[71] Urbain G, Cambier F, Deletter M, Anseau MR. Viscosity of silicate melt. Transactions of the British Ceramic Society 1981;80:139–41.

[72] Dammann M, Mancini M, Kolb T, Weber R. Thermal radiation at high-temperature and high-pressure conditions: Comparison of models for design and scale-up of entrained flow gasification processes. Thermal Sciences and Engineering Progress 2023;40:101772. https://doi.org/10.1016/j.tsep.2023.101772.

[73] Fleck S, Santo U, Hotz C, Jakobs T, Eckel G, Mancini M, Weber R, Kolb T. Entrained flow gasification. Part 1: Gasification of glycol in an atmospheric-pressure experimental rig. Fuel 2018;217:306–19. https://doi.org/10.1016/j.fuel.2017.12.077.

[74] ARTEKA. Glasperlen Strahlmittel. 2021. https://www.arteka.de/Strahltechnik/Glasperlen-Strahlmittel.html.

[75] Mielke K. Über das Verhalten und die Kontrolle von Schlacken des bioliq-Vergasers [Ph.D. thesis]. Aachen, Germany: Fakultät für Maschinenwesen, Rheinisch-Westfälische Technische Hochschule Aachen; Apr 2020. https://doi.org/10.18154/RWTH-2021-10399.

[76] DIN Deutsches Institut für Normung. DIN 51729-11:1998-11. Prüfung fester Brennstoffe. Bestimmung der chemischen Zusammensetzung von Brennstoffasche. Teil 11: Atomemissionsspektrometrische Bestimmung mit induktiv gekoppeltem Plasma (ICP-OES); Nov 1998.

[77] DIN Deutsches Institut für Normung. DIN EN ISO 11885:2009-09. Wasserbeschaffenheit. Bestimmung von ausgewählten Elementen durch induktiv gekoppelte Plasma-Atom-Emissionsspektrometrie (ICP-OES) (ISO 11885:2007); Sep 2009.

[78] Eurofins Umwelt Ost. 2021. https://www.eurofins.de/.

[79] Shen Z, Liang Q, Xu J, Liu H. In situ study on the formation mechanism of bubbles during the reaction of captured chars on molten slag surface. Int J Heat Mass Transf 2016;95:517–24. https://doi.org/10.1016/j.ijheatmasstransfer.2015.12.040.

[80] DIN Deutsches Institut für Normung. DIN 66137-2:2019-03. Bestimmung der Dichte fester Stoffe. Teil 1: Gaspyknometrie; Mar 2019.

[81] Melchior T, Pütz G, Müller M. Surface tension measurements of coal ash slags under reducing conditions at atmospheric pressure. Energy Fuels 2009;23(9):4540–6. https://doi.org/10.1021/ef900449v.

[82] Melchior T, Mueller M. Surface tension measurements of molten coal ash slags under oxidising and reducing gas atmosphere. In: Proceedings of the 8th International Conference on Molten Slags, Fluxes, and Salts, 18–21 January 2009; Santiago, Chile; 2009. p. 161–70. https://www.pyro.co.za/MoltenSlags2009/0161-Melchior.pdf.

[83] Melchior T. Untersuchungen zur Oberflächenspannung von Kohleschlacken unter Vergasungsbedingungen [Ph.D. thesis]. Aachen, Germany: Fakultät für Maschinenwesen, Rheinisch-Westfälische Technische Hochschule Aachen; Dec 2010. http://nbn-resolving.org/urn:nbn:de:hbz:82-opus-34616.

[84] Ebert H-P, Bock V, Nilsson O, Fricke J. The hot-wire method applied to porous materials of low thermal conductivity. High Temperatures – High Pressuress 1993;25(4):391–402.

[85] Ebert H-P, Laudensack B, Hemberger F, Nilsson O, Fricke J. Thermophysical properties of a volcanic rock material. High Temperatures – High Pressures 1998;30(3):261–7.

[86] Ebert H-P, Hemberger F, Fricke J, Büttner R, Bez S, Zimanowski B. Thermophysical properties of a volcanic rock material. High Temperatures – High Pressures 2002;34(5):561–8.

[87] ZAE Bayern. 2021. https://www.zae-bayern.de/index.

[88] Richter F. Die physikalischen Eigenschaften der Stähle: Das 100-Stähle-Programm. Teil I: Tafeln und Bilder; 2012. https://www.tugraz.at/fileadmin/user_upload/Institute/IEP/Thermophysics_Group/Files/Staehle-Richter.pdf.

[89] J + G Feuerfestbau. Data sheet for JUPLAST SM 308 B. SiC mix; Mar 2011.

[90] Gnielinski V. On heat transfer in tubes. Int J Heat Mass Transf 2013;63:134–40. https://doi.org/10.1016/j.ijheatmasstransfer.2013.04.015.

[91] Gnielinski V. Corrigendum to “On heat transfer in tubes”. Int J Heat Mass Transf 2015;81:638. https://doi.org/10.1016/j.ijheatmasstransfer.2014.10.063.

[92] VDI-Gesellschaft Verfahrenstechnik und Chemieingenieurwesen (VDI-GVC). VDI-Wärmeatlas. 12th ed. Berlin, Germany [et al.]: Springer Vieweg; 2019. https://doi.org/10.1007/978-3-662-52989-8.

[93] Dammann M, Mancini M, Weber R, Kolb T. Entrained flow gasification: Numerical simulations of pilot-scale experiments (in preparation). Fuel 2027.

[94] Virtanen P, Gommers R, Oliphant TE, Haberland M, Reddy T, Cournapeau D, Burovski E, Peterson P, Weckesser W, Bright J, van der Walt SJ, Brett M, Wilson J, Millman KJ, Mayorov N, Nelson ARJ, Jones E, Kern R, Larson E, Carey CJ, Polat İ, Feng Y, Moore EW, VanderPlas J, Laxalde D, Perktold J, Cimrman R, Henriksen I, Quintero EA, Harris CR, Archibald AM, Ribeiro AH, Pedregosa F, van Mulbregt P, SciPy 1.0 Contributors. SciPy 1.0: Fundamental algorithms for scientific computing in Python. Nat Methods 2020;17:261–72. https://doi.org/10.1038/s41592-019-0686-2.

[95] SciPy Developers. SciPy. Release 1.5.1; 2021. https://pypi.org/project/scipy/.

[96] Fluegel A. Global model for calculating room-temperature glass density from the composition. J Am Ceram Soc 2007;90(8):2622–5. https://doi.org/10.1111/j.1551-2916.2007.01751.x.

[97] Lyon KC. Calculation of surface tensions of glasses. Journal of the America Ceramic Society 1944;27(6):186–9. https://doi.org/10.1111/j.1151-2916.1944.tb14889.x.

[98] Boni RE, Derge G. Surface tensions of silicates. Journal of Metals 1956;8(1):53–9. https://doi.org/10.1007/bf03377643.

[99] Goleus VI, Belyi AY, Sardak EM, Belyi YI. Calculation of the surface tension of molten borosilicate glasses. Glass and Ceramics 1996;53(7–8):226–8. https://doi.org/10.1007/BF01213775.

[100] Kucuk A, Clare AG, Jones L. An estimation of the surface tension for silicate glass melts at 1400 °C using statistical analysis. Glass Technology 1999;40(5):149–53. https://www.ingentaconnect.com/content/sgt/gt/1999/00000040/00000005/4005149.

[101] Lange RA. A revised model for the density and thermal expansivity of K_2O–Na_2O–CaO–MgO–Al_2O_3–SiO_2 liquids from 700 to 1900 K: Extension to crustal magmatic temperatures. Contributions to Mineralogy and Petrology 1997;130(1):1–11. https://doi.org/10.1007/s004100050345.

[102] Fluegel A, Earl DA, Varshneya AK, Seward TP. Density and thermal expansion calculation of silicate glass melts from 1000 °C to 1400 °C. Physics and Chemistry of Glasses – European Journal of Glass Science and Technology, Part B 2008;49(5):245–57. https://www.ingentaconnect.com/content/sgt/ejgst/2008/00000049/00000005/art00003.

[103] Wu G, Yazhenskikh E, Hack K, Wosch E, Müller M. Viscosity model for oxide melts relevant to fuel slags. Part 1: Pure oxides and binary systems in the system SiO_2–Al_2O_3–CaO–MgO–Na_2O–K_2O. Fuel Process Technol 2015;137:93–103. https://doi.org/10.1016/j.fuproc.2015.03.025.

[104] Wu G, Yazhenskikh E, Hack K, Müller M. Viscosity model for oxide melts relevant to fuel slags. Part 2: The system SiO_2–Al_2O_3–CaO–MgO–Na_2O–K_2O. Fuel Process Technol 2015;138:520–33. https://doi.org/10.1016/j.fuproc.2015.06.031.

[105] Wu G. Modelling and experimental validation of the viscosity of liquid phases in oxide systems relevant to fuel slags [Ph.D. thesis]. Aachen, Germany: Fakultät für Maschinenwesen, Rheinisch-Westfälische Technische Hochschule Aachen; Jun 2015. https://doi.org/10.18154/RWTH-2015-05568.

[106] Wu G, Seebold S, Yazhenskikh E, Hack K, Müller M. Viscosity model for oxide melts relevant to fuel slags. Part 3: The iron oxide containing low order systems in the system SiO_2–Al_2O_3–CaO–MgO–Na_2O–K_2O–FeO–Fe_2O_3. Fuel Process Technol 2018;171:339–49. https://doi.org/10.1016/j.fuproc.2017.09.002.

[107] Wu G, Seebold S, Yazhenskikh E, Tanner J, Hack K, Müller M. Slag mobility in entrained flow gasifiers optimized using a new reliable viscosity model of iron oxide-containing multicomponent melts. Appl Energy 2019;236:837–49. https://doi.org/10.1016/j.apenergy.2018.11.100.

[108] Ozawa S, Susa M. Effect of Na_2O additions on thermal conductivities of CaO–SiO_2 slags. Ironmaking & Steelmaking 2005;32(6):487–93. https://doi.org/10.1179/174328105x48179.

[109] Ozawa S, Endo R, Susa M. Thermal conductivity measurements and prediction for R_2O–CaO–SiO_2 (R = Li, Na, K) slags. Tetsu-to-hagane 2007;93(6):416–23. https://doi.org/10.2355/tetsutohagane.93.416.

[110] Choudhary MK, Potter RM, Heat transfer in glass-forming melts. In: Joseph I, Montenero A, editors. Properties of glass-forming melts; Boca Raton, FL, USA: CRC Press; 2005. vol. 9, p. 249–94.

[111] Potters Industries. Properties of A & E glass. 2016.

[112] Stebbins JF, Carmichael ISE, Moret LK. Heat capacities and entropies of silicate liquids and glasses. Contributions to Mineralogy and Petrology 1984;86(2):131–48. https://doi.org/10.1007/bf00381840.

[113] Cao X, Kong L, Bai J, Ge Z, He C, Li H, Bai Z, Li W. Effect of water vapor on coal ash slag viscosity under gasification condition. Fuel 2019;237:18–27. https://doi.org/10.1016/j.fuel.2018.09.137.

[114] Gong Y, Zhang Q, Guo Q, Xue Z, Wang F, Yu G. Vision-based investigation on the ash/slag particle deposition characteristics in an impinging entrained-flow gasifier. Appl Energy 2017;206:1184–93. https://doi.org/10.1016/j.apenergy.2017.10.037.

[115] Yuan H, Wang F, Yu Z. Heat transfer calculation of composite lining in gasifier. Coal Conversion 2004;27(4):21–6. https://oversea-1cnki-1net-1woyhhav906f0.erf.sbb.spk-berlin.de/kcms/detail/detail.aspx?dbcode=CJFD&filename=MTZH200404004&dbname=CJFD2004.

[116] Santo U, Böning D, Eberhard M, Schmid H, Kolb T. Entrained flow gasification: Experiments and balancing for design and scale-up. In: Proceedings of the 30th Deutscher Flammentag: für nachhaltige Verbrennung, 28–29 September 2021; Hannover-Garbsen, Germany: Deutsche Vereinigung für Verbrennungsforschung and The Combustion Institute Deutsche Sektion; 2021. https://doi.org/10.5445/IR/1000139705.